Acta Pharmaceutica Sinica B 2021;11(10):3244–3261

Chinese Pharmaceutical Association
Institute of Materia Medica, Chinese Academy of Medical Sciences

Acta Pharmaceutica Sinica B

www.elsevier.com/locate/apsb
www.sciencedirect.com

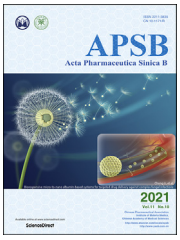

ORIGINAL ARTICLE

# Self-assembled FeS-based cascade bioreactor with enhanced tumor penetration and synergistic treatments to trigger robust cancer immunotherapy

**Hao Ren[a,*,†], Jiahui Yong[a,†], Qingqing Yang[a], Zhen Yang[a], Zhangya Liu[a], Yan Xu[a], Hao Wang[a], Xing Jiang[b], Wenjun Miao[a], Xueming Li[a,*]**

[a]*School of Pharmaceutical Science, Nanjing Tech University, Nanjing 211816, China*
[b]*School of Nursing, Nanjing University of Chinese Medicine, Nanjing 210023, China*

Received 1 April 2021; received in revised form 28 April 2021; accepted 6 May 2021

**KEY WORDS**

FeS-based cascade bioreactor;

**Abstract** Major challenges for cancer treatment are how to effectively eliminate primary tumor and sufficiently induce immunogenic cell death (ICD) to provoke a robust immune response for metastasis control. Here, a self-assembled cascade bioreactor was developed to improve cancer treatment with enhanced tumor penetration and synergistic therapy of starvation, chemodynamic (CDT) and

*Abbreviations:* ALT, alanine transaminase; ATP, adenosine triphosphate; AST, aspartate aminotransferase; ALP, alkaline phosphatise; BUN, blood urea nitrogen; CDT, chemodynamic therapy; Ce6, Chlorin e6; CLSM, confocal laser scanning microscope; CREA, creatinine; CRT, calreticulin; CTLA-4, cytotoxic T-lymphocyte-associated protein 4; CTLs, cytotoxic T lymphocytes; DAMPs, damage-related molecular patterns; DAPI, 2-(4-amidinophenyl)-6-indolecarbamidine dihydrochloride; DCs, dendritic cells; DLS, dynamic light scattering; DMPO, dimethyl pyridine *N*-oxide; EDS, energy-dispersive spectrometry; EPR, enhanced permeability and retention; EDC, 1-ethyl-3-(3′-dimethylaminopropyl) carbodiimide; ESR, electron spin resonance; FG, FeS-GOx nanodots; FGP, FeS-GOx@PTX nanoparticles; FITC, fluorescein Isothiocyanate; $FeCl_2 \cdot 4H_2O$, iron dichloride tetrahydrate; Glu, glucose; GOx, glucose oxidase; $H_2$DCFDA, 2,7-dichlorodihydrofluorescein acetoacetic acid; H&E, hematoxylin and eosin; HMGB-1, high mobility group box protein 1; HSA, human serum albumin; HPF, 2-[6-(4,-hydroxy) phenoxy-3*H*-xanthene-3-on-9-yl; ICB, immune checkpoint blockade; ICD, immunogenic cell death; IFN-γ, interferon-γ; MB, methylene blue; MCTS, multicellular tumor spheroids; MFI, median fluorescence Intensity; $Na_2S$, sodium sulfide; NHS, *N*-hydroxy succinimide; OH, hydroxyl; PBS, phosphate buffer saline; PTT, photothermal therapy; PTX, paclitaxel; ROS, reactive oxygen species; SEM, scanning electron microscope; TAA, tumor-associated antigens; TDLN, tumor-draining lymph nodes; TEM, transmission microscope; TMB, 3,3′,5,5′-tetramathylbenzidine; TUNEL, terminal deoxynucleotidyl transferase dUTP nick end labelling; XPS, X-ray photoelectron spectroscopy; XRD, X-ray diffraction patterns.

*Corresponding authors.
E-mail addresses: Hren@njtech.edu.cn (Hao Ren), Xuemingli@njtech.edu.cn (Xueming Li).
†These authors made equal contributions to this work.

Peer review under responsibility of Institute of Materia Medica, Chinese Academy of Medical Sciences and Chinese Pharmaceutical Association.

https://doi.org/10.1016/j.apsb.2021.05.005

Glucose oxidase;
Tumor penetration;
Synergistic therapy;
ICD amplifier;
Cancer immunotherapy;
Metastasis inhibition

photothermal therapy. Ultrasmall FeS-GOx nanodots were synthesized with glucose oxidase (GOx) as template and induced by paclitaxel (PTX) to form self-assembling FeS-GOx@PTX (FGP) *via* hydrophobic interaction. After accumulated at tumor sites, FGP disassembles to smaller FeS-GOx for enhanced deep tumor penetration. GOx maintains high enzymatic activity to catalyze glucose with assistant of oxygen to generate hydrogen peroxide ($H_2O_2$) as starvation therapy. Fenton reaction involving the regenerated $H_2O_2$ in turn produced more hydroxyl radicals for enhanced CDT. Following near-infrared laser at 808 nm, FGPs displayed pronounced tumor inhibition *in vitro* and *in vivo* by the combination therapy. The consequent increased exposure to calreticulin amplified ICD and promoted dendritic cells maturation. In combination with anti-CTLA4 checkpoint blockade, FGP can absolutely eliminate primary tumor and avidly inhibit distant tumors due to the enhanced intratumoral infiltration of cytotoxic T lymphocytes. Our work presents a promising strategy for primary tumor and metastasis inhibition.



## 1. Introduction

Immune checkpoint blockade (ICB) based cancer immunotherapy is an attractive strategy for recurrent and metastasized cancer, due to the activation of anti-tumor immune response[1−3]. Despite the remarkable progress in clinical cancer treatment, only a subset of cancer patients (5%−20%) show immune response with ICB therapy, because of the weak tumor immunogenicity and insufficient intratumoral infiltration of cytotoxic T lymphocytes (CTLs)[4,5]. The introduction of immunogenic cell death (ICD) has been proved as a promising approach to reverse tumor immunosuppression[6−8]. Dying tumor cells undergoing ICD can trigger a specific anti-tumor immune response by the release of tumor-associated antigens and damage-related molecular patterns (DAMPs), which promote the activation of dendritic cells (DCs) and recruit specific T cell engagement[9−11]. Therefore, efficient approaches that destroy primary tumor and amplify ICD to provoke an immune response for eradication of metastasis are highly desirable.

Intracellular reactive oxygen species (ROS) can induce cellular oxidative damage that effectively induces ICD to provide antigenic stimulation for the immune system[12−14]. The Fenton reaction based chemodynamic therapy (CDT) can release iron (Fe) ions to catalyze the overexpression of hydrogen peroxide ($H_2O_2$). This results in the generation of hydroxyl radicals (·OH) in primary cancer treatment[15−17]. The pronounced toxicity of ·OH can also trigger antigens release and regulates immunogenicity to promote maturation of DCs, thereby increasing the anti-tumor immune response[18−20]. Thus, triggering sufficient ROS by CDT is suitable to amplify ICD and enhance ICB immunotherapy. However, the reaction kinetic of the Fenton reaction-based CDT is highly dependent on the performance of catalysts and reaction parameters[21]. The mildly acid (pH 5 to 6) and insufficient level of $H_2O_2$ in tumor microenvironment may limit the CDT-induced ICD process for cancer immunotherapy[22−24].

To overcome these problems, glucose oxidase (GOx) has been proposed to increase intracellular $H_2O_2$ concentration and decrease pH, thus accelerating the Fenton reaction to generate highly cytotoxic ·OH for enhanced CDT[25,26]. GOx is an endogenous oxides-reductase that selectively catalyze glucose to generate gluconic acid and $H_2O_2$ in the presence of oxygen[27,28]. Due to Warburg effect, tumor cells consume more glucose for cancer growth. Therefore, the GOx could block glucose and oxygen supply to achieve tumor inhibition as starvation therapy[29,30]. In addition, Sun groups have found that the delivery of GOx with biomimetic nanoparticles could ablate tumors and facilitate DCs maturation to stimulate antitumor immune response by starvation therapy[31,32]. In the nearby of tumor blood vessels with oxygen supply, GOx-based starvation therapy could enhance CDT and the combination strategy could be used to amplify ICD to increase ICB immunotherapy in some degree. However, due to the increased tumor depth and oxygen consumption, hypoxia of tumor microenvironment was significantly enhanced and restricted the catalyze efficacy of GOx[33−36], resulting in unsatisfied primary tumor inhibition and an insufficient immune response. Therefore, we hypothesize that the combination of oxygen-independent photothermal therapy (PTT) would further eliminate residual cancer cells and induce sufficient ICD to provoke a robust anti-tumor immune response for ICB enhancement.

PTT can transfer light energy to heat and induce tumor cell apoptosis with hyperthermia for local cancer treatment[37]. Recent studies have indicated that PTT can promote ICD induction and the release of DAMPs to increase tumor immunogenicity, thereby enhancing the anti-tumor immune response[38−40]. In addition, numerous pieces of evidence have also demonstrated the GOx activity can be strengthened along with increased temperature[41]. Thus, the photothermal effect of PTT could also enhance GOx-based starvation therapy and generate more $H_2O_2$ to accelerate ·OH radicals for CDT enhancement. The combination therapy could effectively inhibit the progression of the primary tumor and induce strong anti-tumor response for metastatic tumor cells.

Unlike organic photosensitizers (indocyanine green, IR780, and others) easily to photo-quench, ultrasmall FeS nanodots can generate localized heat as PTT and also catalyze $H_2O_2$ to produce ·OH as CDT[42,43]. They were synthesized with use human serum albumin (HSA) protein as template by a facile enzyme-biomimetic route at room temperature. Inspired by this mild biomineralization method[44,45], we utilized GOx instead of HSA to form FeS-GOx nanodots. It has been reported that the smaller nanodots could penetrate deeper at tumor site due to the reduced diffusional obstacle[46−48]. The designed FeS-GOx nanodots could meet the demands of combined multi-therapy for primary tumor inhibition with higher deep penetration and induction of sufficient ICD for tumor immunotherapy enhancement. However, ultrasmall

nanodots are quickly eliminated from body by the kidney, which results in short blood circulation time and reduced tumor accumulation[49].

Considering this obstacle, the chemotherapy drug paclitaxel (PTX) as a model drug was introduced *via* hydrophobic interaction during the co-assembly of FeS-GOx nanodots to form larger FeS-GOx@PTX (denote as FGP; Fig. 1A). After intravenous injection, the larger FGP nanoparticles could effectively accumulate in tumors by the enhanced permeability and retention (EPR) effect. Subsequently, due to the acid tumor microenvironment, the FGP could disassemble to release PTX and smaller FeS-GOx nanodots for deeper penetration (Fig. 1B). The released PTX could induce tumor cell apoptosis for chemotherapy. In nearby of tumor blood vessels, GOx in FGP still maintained high enzymatic activity to catalyze glucose and produce $H_2O_2$ with assistant of oxygen, shutting down nutrients supply as starvation therapy. The generation $H_2O_2$ could accelerate Fenton reaction to produce more ·OH radicals for enhanced CDT (Fig. 1C). After near-infrared (NIR) laser irradiation (808 nm), the increased temperature of FGP-based PTT could strengthen GOx activity and result in starvation and CDT enhancement. In addition, with the increased tumor penetration of FeS-GOx nanodots, PTT could effectively kill deeper hypoxic tumors for primary tumor inhibition. So, the designed nanoparticles showed significant tumor inhibition with PTX-induced chemotherapy, PTT, starvation therapy and CDT. In addition, the synergistic therapy involving FGP amplified the induction of ICD to exposure calreticulin (CRT) expression on dying tumor cells, which induced DC maturation. Furthermore, in combination with the cytotoxic T-lymphocyte-associated protein 4 (CTLA4) checkpoint blockade, FGP could significantly promote intratumoral infiltration of CTLs into distant tumors and inhibit growth (Fig. 1D). Taken together, the presently designed self-assembling FGP nano-reactor can effectively and synergistically eliminate primary tumor with deeper tumor penetration and can amplify ICD to active strong anti-tumor response for metastasis inhibition.

## 2. Materials and methods

### 2.1. *Materials*

Glucose oxidase (GOx) was purchased from Source Leaf Biotechnology Co., Ltd. (Shanghai, China). PTX and chlorin e6 were provided by Dalian Meilun Biotechnology Co., Ltd. (Dalian, China). The fluorimetric hydrogen peroxide assay kit was provided by Sigma−Aldrich. (St. Louis, MO, USA). The cell counting kit-8 (CCK-8) and annexin V-fluorescein isothiocyanate, FITC apoptosis detection kit were obtained from Dojindo Laboratories (Kumamoto, Japan). HPF (2-[6-(4,-hydroxy) phenoxy-3*H*-xanthene-3-on-9-yl] benzoic acid) was obtained from Cayman Chemical (Ann Arbor, MI, USA). Anti-mouse-CD11c-FITC, anti-mouse-CD80-APC, anti-mouse-CD86-PE, anti-mouse-CD3-APC, anti-mouse-CD8-PE were bought from BioLegend (San Diego,

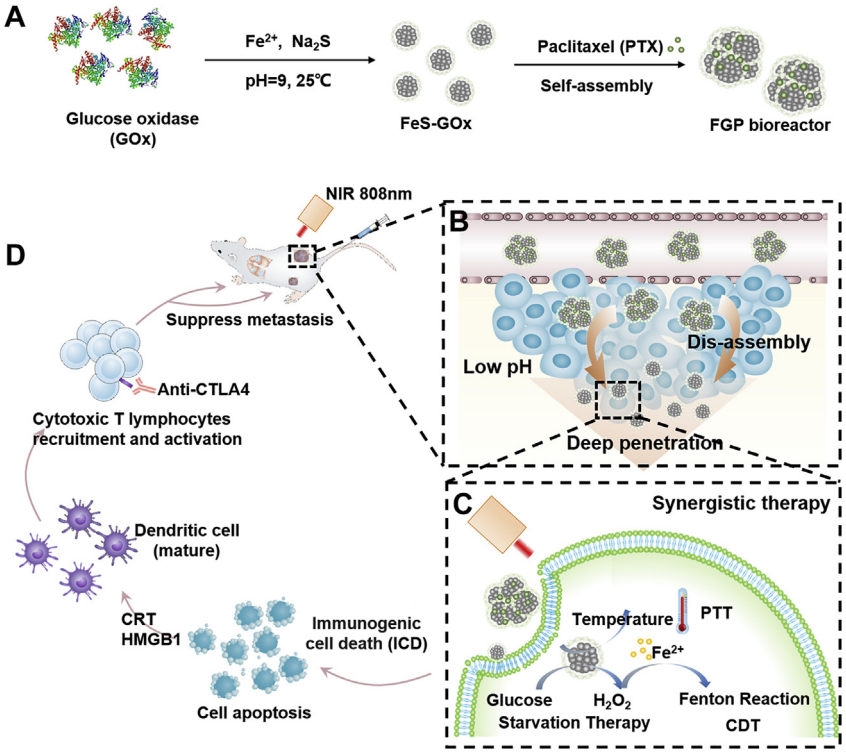


**Figure 1** Schematic illustration of the synthetic process and therapeutic mechanism of the cascade bioreactor. (A) Construction process of the FGP bioreactor *via* enzyme-biomimetic route and drug-induced self-assembly method. (B) Illustration of FGP disassembly for deep tumor penetration. (C) Synergistic therapy of starvation therapy, CDT and PTT for primary tumor inhibition. (D) Synergistic therapy releases damage-related molecular patterns to amplify ICD for enhanced anti-tumor immunotherapy.

CA, USA). CRT antibody, HMGB-1 antiboby were bought from Dakewe Biotech Co., Ltd. (Shenzhen, China) and secondary antibody was purchased from Shanghai Abways Biotechnology Co., Ltd. (Shanghai, China). Anti-CTLA-4 antiboby was purchased from Bio X Cell (West Lebanon, New Hampshire, USA). IFN-γ antibody and Foxp3 antibody were obtained from Proteintech Group Co., Ltd. (Wuhan, China). Alanine aminotransferase (ALT), aspartate aminotransferase (AST), alkaline phosphatase (ALP), blood urea nitrogen (BUN), and creatinine (CREA) kits were purchased from Jiancheng Bioengineering Institute (Nanjing, China).

### 2.2. Synthesis of FeS-GOx nanodots

FeS-GOx nanodots were synthesized and simply modified by the previously described biomineralization method[43]. Briefly, 20 mg GOx was dissolved in 2 mL deionized water, followed by the gradual addition of $FeCl_2.4H_2O$ (30 mmol/L) with constant stirring. The pH was adjusted to 8.0 with NaOH (0.01 mol/L). Subsequently, $Na_2S$ solution (32 mmol/L) was added and samples were constantly stirred at 25 °C for 2 h. Finally, the FeS-GOx was obtained by dialysis for 12 h. The preparation procedure of FeS-HSA was similar as the synthesis method of FeS-GOx. In order to avoid the oxidizing of $Fe^{2+}$, in the process of preparation, all addition chemicals were disolved in degassed water and under the flow with $N_2$.

### 2.3. Synthesis of FeS-GOx@PTX (FGP) and FeS-HSA@PTX (FHP)

FGP was constructed by the self-assembly of FeS-GOx induced by PTX as previously described[50]. PTX in ethanol (10 mg/mL, 1 mL) ethanol solution was added to 2 mL of FeS-GOx solution and then mixed for 1 h to allow the formation of FGP nanoparticles. The supernatant was collected centrifugation at 10,000 rpm (GL-20G-II, Anting Scientific, Shanghai, China) centrifugation for 10 min and washed twice with water. Finally, excess PTX was removed by a 12-h dialysis. The obtained FGP was stored in 4 °C for further use. In order to evaluate the starvation therapy and $H_2O_2$ generation, FeS-HSA was instead of FeS-GOx to form FeS-HSA@PTX (denoted FHP). The preparation was similar as that of FGP.

### 2.4. Characterization of FGP

The concentration of GOx was determined using the BCA protein assay kit (Beyotime Biotechnology, Nanjing, China). The concentration of Fe was determined according to the ultraviolet−visible (UV−Vis) absorption spectrum using 2-2′ dipyridyl as a chromogenic agent. The concentration of PTX was analyzed by high-performance liquid chromatography (HPLC) (Shimadzu, Kyoto, Japan). The morphology and structure of nanoparticles were characterized by a transmission microscopy using a JEM-2100 microscope (JEOL, Tokyo, Japan). The stability of FGP nanoparticles suspended in PBS was determined by monitoring the particles size and surface zeta potential by dynamic light scattering (DLS) using a Zetasizer Nano ZS-90 (Malvern Instruments, Malvern, UK). The disassembly of FGP was performed at pH 5.0 and pH 7.4 for 24 h. The size distribution of the disassembled nanoparticles was determined by DLS (Malvern). The chemical valences of the Fe elements were analyzed by X-ray photoelectron spectroscopy (XPS) using an ESCAlab250 electron spectrometer (Thermal Fisher Scientific, Waltham, MA, USA). The generation of hydroxyl free radicals (·OH) was recorded on an A300 electron spin resonance (ESR) spectrometer (Bruker, Leipzig, Germany) using 5,5-dimethyl-1-pyrroline *N*-oxide (DMPO) as the spin trapping agent.

### 2.5. Catalytic activity of FGP

Catalytic activity of FGP was mainly evaluated by pH variation, oxygen consumption and $H_2O_2$ generation. Briefly, a series of FGP concentrations were added to 3 mL phosphate buffer. Following the addition with glucose (2 mg/mL), the variation in the oxygen concentration variation was detected by a real-time portable dissolved oxygen analyzer (Leici Co., Ltd., JPB-607 A, Shanghai, China) and the pH variation was immediately monitored by a pH meter (Leici Co., Ltd., PHSJ-5, Shanghai, China). Additionally, the generation of $H_2O_2$ was determined by Fluroimetric Hydrogen Peroxide Assay Kit according to the standard protocols. To demonstrate the influence of temperature on enzymatic activity, 10 μg GOx (0.2 mg/mL, 50 μL) was added into a glucose solution (9 mg/mL), then the reaction was processed under different temperature conditions from 25 to 70 °C for 15 min. The pH changes of the mixture of FGP (200 μg/mL) and glucose (9 mg/mL) under different temperature at 25, 37, 42, and 47 °C was detected.

### 2.6. In vitro PTX release study

FGP samples (2 mL) containing 1 mg/mL PTX were dialyzed against 40 mL PBS (pH = 7.4 or pH = 5.8) containing 0.2% (*w*/*v*) Tween-80 at 37 °C with constant shaking at 100 rpm. At specific time intervals, 2 mL of the dialysis solution was removed and an equal volume of fresh PBS was added at the same time. And then, the concentration of PTX was analyzed by HPLC (Shimadzu) using a water/acetonitrile mixture (45/55, *v*/*v*).

### 2.7. In vitro photothermal study

In order to evaluate the photothermal performance of FGP, 0.2 mL FGP samples containing 200, 300 or 600 μg/mL Fe were NIR irradiated at 808 nm using a laser operating (Leilan Co., Ltd., Wuhan, China) at a power density of 1.6 W/cm$^2$. The temperature was recorded every 1 min by a thermometer. The photo-stability of FGP was measured during five cycles of irradiation (5 min for each cycle).

### 2.8. Detection of ·OH generation

Methylene blue (MB) decolorization was used to determine ·OH generation. MB (10 μg/mL) was added into FGP solutions containing 30 μg/mL Fe and 300 μg/mL GOx, followed with addition of glucose (10 mg/mL). The absorption changes at 665 nm were determined at different times using a model UV-2450 UV−Vis spectrophotometer (Shimadzu, Kyoto, Japan). The same method was also used to evaluate ·OH generation of FGP (100 μg/mL) in buffers with a pH 5.0, 6.5 or 7.4. In addition, the temperature of the water bath that was used was increased to 42 °C to simulate the photothermal effect of FGP with NIR laser to assess the enhanced generation ·OH.

3,3′,5,5′-Tetramathylbenzidine (TMB) can be oxidized by ·OH to form the blue oxide of TMB (oxTMB). Based on this observation, the TMB chromogenic method was also used for ·OH

detection. Briefly, TMB (3.2 mmol/L), FGP containing 10 μg/mL Fe and glucose (10 mg/mL) were added into 3 mL of sodium acetate buffer (pH = 5.2). The mixture was incubated at room temperature for 4 h and the UV−Vis spectra (Shimadzu) were recorded. To further clarify the generation of ·OH, DMPO was used to trap ·OH radicals, followed by ESR detection. The DMPO (0.2 mg/mL) was dispersed in glucose (10 mg/mL), FGP (Fe, 50 μg/mL) was added and ESR analysis was performed 30 min later.

### 2.9. *In vitro cytotoxicity*

The *in vitro* cancer cell cytotoxicity induced by the Fenton reaction, starvation therapy, and the combination therapy with FGP was evaluated in 4T1 breast cancer tumor cells. In brief, 4T1 cells were seeded at a density of 8000 cells per well in 96-well plates and incubated overnight. The cells were untreated (PBS added) or treated with different concentrations of FGP for 4 h in DMEM medium with or without glucose. To create a hypoxic condition, 30 μL-paraffin was added to cover the surface of the medium for 3 h. The oxygen content was approximately about 3%−5%. After normoxia or hypoxia for 4 h at 37 °C under normoxia or hypoxia, the supernatant was removed and carefully washed twice with PBS, followed by the addition of a mixture of CCK-8 (10 μL) and fresh medium (100 μL). After incubation for another 2 h, the cell viability was analyzed by measuring the absorbance at 450 nm by an Infinite F50 microplate reader (Tecan Life Sciences, Männedorf, Switzerland). The effect of the combination therapy involving FGP evaluated similarly. The different concentrations of FGP and FHP (0.01 mg/mL or 0.02 mg/mL GOx and Fe concentration of 100 and 200 μg/mL) were incubated for 4 h prior to PTT by NIR laser irradiation (808 nm, 1.6 W/cm$^2$, 3 min).

Flow cytometry was performed to examine cell apoptosis analysis to evaluate the therapeutic efficacy of FGP. The procedure was similar to the cytotoxicity evaluation. 4T1 tumor cells were incubated with fresh medium containing FGP (0.015 mg/mL GOx and Fe concentration of 150 μg/mL) in a six-well plate. After incubation for 4 h, with or without laser irradiation (808 nm, 1.6 W/cm$^2$, 3 min), the cells were collected and rinsed. The cells were then dispersed in Annexin V Binding Solution and stained with the Annexin V-FITC/PI Apoptosis Detection Kit and immediately analyzed by flow cytometry (ACEA Biosciences, San Diego, CA, USA). For calcein acetomethoxy/propidium iodide (AM/PI) staining, the cytotoxicity of FGP and FHP (0.02 mg/mL GOx and Fe concentration of 200 μg/mL) were stained by a fluorescent dying mixture consisting of PI solution (8 μmol/L) and Calcein-AM (2 μmol/L). After incubation for 15 min, fluorescence microscopy images of cells were obtained (Nikon, Tokyo, Japan).

### 2.10. *Cellular uptake and three-dimensional (3D) tumor penetration of FGP in vitro*

To evaluate the cellular uptake and 3D tumor penetration of FGP, the Ce6 fluorescence dye was applied to label FGP. 1-Ethyl-3-(-3-dimethylaminopropyl) carbodiimide hydrochloride (EDC)/*N*-hydroxysuccinimide (NHS) were used to active Ce6 and conjugate it to FGP. The 4T1 cells were seeded in six-well plates at a density of $1 \times 10^6$ cells per well and incubated at 37 °C overnight. Ce6-labeled FGP (Ce6, 1 μg/mL) was added and incubated for 0.5, 1 or 2 h. The cells were detached, collected and washed with PBS and lastly suspended in PBS for analysis using a flow cytometry analysis (ACEA Biosciences). The 3D multicellular tumor spheroids were constructed by incubating 4T1 cells ($5 \times 10^3$ per well) into ultralow attachment round-bottom 96-cell plates (Corning, 7007; Corning, New York, NY, USA). After the spheroid reached 400 μm, Ce6-labeled FGP (Ce6, 1 μg/mL) was incubated in different conditions (pH 7.4 and pH 6.0) for 24 h. Then, the 3D tumor spheroids were transferred to confocal dishes and finally, the fluorescence images of Ce6 was captured by confocal laser scanning microscopy (CLSM) (Nikon) was performed in an XY-stack at 10-μm intervals.

### 2.11. *Intracellular generation of ROS and ·OH*

The fluorescence detection probes carboxy-2′,7′-dichlorodihydrofluorescein diacetate (carboxy-$H_2$DCFDA) with excitation (Ex) and emission (Em) wavelengths of 495 and 525 nm, respectively, and HPF (Ex/Em = 490/515 nm) were applied to respectively evaluate the intracellular ROS and ·OH level in 4T1 tumor cells, respectively. In brief, 4T1 cells were treated with FGP or FHP (with an equivalent Fe concentration of 180 μg/mL) for 2 h. The cells were rinsed and stained with carboxy-$H_2$DCFDA (20 μmol/L in serum-free medium) and HPF (10 μmol/L) at 37 °C for 30 min. The cells were then fixed in 4% formaldehyde polymer and labeled with 4′,6-diamidino-2-phenylindole (DAPI, 1 μg/mL), and washed twice with PBS. Finally, the fluorescence images of cells were captured by a fluorescence microscopy and the mean fluorescence was calculated by Image J software (NIH, Bethesda, MD, USA). The ROS generation was also similarly evaluated by flow cytometry (ACEA Biosciences) using 4T1 cells seeded in six-well plates ($1 \times 10^6$ cells) per well, centrifuged when required, and suspended in PBS for analysis.

### 2.12. *In vitro detection of $H_2O_2$*

The generation of $H_2O_2$ *in vitro* was measured by the Fluorimetric Hydrogen Peroxide Assay Kit according to the standard protocols. The 4T1 tumor cells (8000 per well) were permitted to adhere overnight. After 2-h treatment with RPMI 1640 medium containing various concentrations of FGP (GOx 0.02, 0.05, or 0.1 mg/mL), the cells were washed twice with PBS and stained with Fluorimetric Hydrogen Peroxide Assay Kit for 15 min. Finally, fluorescence (Ex/Em = 540/590 nm) was detected by the VICTOR Nivo multimode microplate reader (PerkinElmer, Waltham, MA, USA).

### 2.13. *In vitro detection of CRT expression*

To evaluate the ICD amplifier, CRT expression on the surface of 4T1 tumor cells was determined by immunofluorescence staining. The 4T1 cells were incubated in six-well plates at a density of $1 \times 10^6$ per well and after incubation for 24 h. The cells were treated with PBS, FGP and FHP (GOx 100 μg/mL, Fe 180 μg/mL) for 3 h. After NIR irradiation (808 nm, 1.6 W/cm$^2$, 3 min), the cells were incubated with CRT primary antibody and fluorochrome-conjugated secondary antibody according to the standard protocols. Fluorescence images were captured by a fluorescence microscope (Nikon). The mean fluorescence intensity was calculated based on Image J software (NIH).

### 2.14. *In vitro determination of HMGB-1 and ATP*

The cellular high mobility group box 1 (HMGB-1) were evaluated by a HMGB-1 ELISA kits according to the manufacture's

protocol. Briefly, 4T1 cells were seeded in 12-well plates at a density of $5 \times 10^5$ cells per well and incubated overnight. After treatment with FHP and FGP (GOx 50 μg/mL, Fe 180 μg/mL) for 3 h, the 4T1 cells were irradiated with an 808 nm laser (1.6 W/cm$^2$) for 3 min. Finally, the supernatant was centrifuged for HMGB-1 analysis by an ELISA kit (Tongwei, Shanghai, China). In addition, the release of adenosine triphosphate (ATP) in the extracellular environment was determined by bioluminescence assays. The 4T1 cells ($1 \times 10^6$ per well) were seeded in six-well plates and incubated for 24 h in advance. Then, the cells were treated with PBS, FHP and FGP (GOx 25 μg/mL, Fe 180 μg/mL) for 3 h. After NIR irradiation (808 nm, 1.6 W/cm$^2$, 3 min), the cell supernatant was collected and centrifuged at 2500 rpm (LGJ-10C, Foring technology, Beijing, China) for 5 min. Then, the extracellular ATP was determined using ATP assay kit (Beyotime, Nanjing, China) and light emission was measured with Multimode board reader (VICTOR NIVO™).

### 2.15. Intracellular $Fe^{2+}$ determination

The intracellular $Fe^{2+}$ was evaluated by FerroOrange (Ex/Em = 490/515 nm) (Dojindo, Tokyo, Japan), which is a novel fluorescent probe that enables live-cell fluorescent imaging of $Fe^{2+}$. Briefly, 4T1 cells were seeded in 12-well plates at a density of $5 \times 10^5$ cells per well and incubated overnight. After incubation with FHP and FGP (GOx 25 μg/mL, Fe 180 μg/mL) for 3 h, the 4T1 cells were labeled with FerroOrange (1 μmol/L) working solution for another 30 min. Finally, the fluorescence of $Fe^{2+}$ in 4T1 cells was observed under a confocal fluorescence microscope (OLYMPUS, FV1000, Tokyo, Japan).

### 2.16. Animals and tumor model

Six-week-old female BALB/c mice were provided by Yangzhou University Medical Center (Yangzhou, China). All animal procedures were performed in accordance with the Guidelines for Care and Use of Laboratory Animals of Nanjing Tech University. All experimental procedures were executed according to the protocols approved by the Animal Ethics Committee of Jiangsu Center for Safety Evaluation of Drugs. Cultured 4T1 cells ($1 \times 10^7$/mL) were injected into right flank of mice to generate the 4T1 tumor-bearing mice model.

### 2.17. In vivo fluorescence imaging and biodistribution analysis of FGP

For NIR fluorescence imaging, Ce6-labeled FeS-GOx nanodots and FGP (0.2 mL, Ce6, 300 μg/mL) were intravenously injected into 4T1 tumor bearing mice when the tumors reached about 100 mm$^3$. Fluorescence images of Ce6 (Ex/Em = 675/740 nm) in mice was obtained using the Maestro system (Cri Inc., Woburn, MA, USA) at 2, 6, 8, 10, 12, 24, 36 and 48 h. After imaging, the mice were sacrificed and major organs were excised for *ex vivo* imaging. Ce6 fluorescence data were analyzed using IVIS Living imaging software (PerkinElmer, New York, NY, USA).

In order to investigate the enhancement of the penetration of FGP *in vivo*, Ce6-labeled FGP (0.2 mL, Ce6, 300 μg/mL) were intravenously injected into 4T1 tumor bearing mice when the tumors reached about 100 mm$^3$. The tumors were collected after 24 h and frozen sections of each tumors were stained with DAPI. Finally, the fluorescence images of Ce6 (Ex/Em = 640/710 nm) were captured by fluorescence microscope (Nikon).

### 2.18. In vivo analysis of $Fe^{2+}$ in tumor

The $Fe^{2+}$ level *in vivo* within the tumor was evaluated by Iron assay kit. Briefly, when the tumor size reached approximately 100−150 mm$^3$, FGP (GOx 300 μg/mL, Fe 500 μg/mL) and saline were intravenously injected into 4T1 tumor-bearing mice ($n = 3$). Thereafter, all mice were sacrificed and the tumors were collected after 24 h post-injection. To measure the $Fe^{2+}$ content, the tumors were weighed and homogenized in 1 mL of ice-cold PBS by a homogenizer and centrifuged (16,000×*g*) (Foring technology) for 10 min at 4 °C. Then, the level of $Fe^{2+}$ in the supernatants were determined by the corresponding Iron Assay Kits (Dojindo, Tokyo, Japan) according to the manufacture's instructions.

### 2.19. In vivo photothermal effect

The photothermal effect of FGP was evaluated when tumor volumes reached approximately 100 mm$^3$. The tumor-bearing mice were intravenously injected with saline, FHP and FGP (containing GOx 300 μg/mL and Fe 500 μg/mL) and NIR laser irradiated (808 nm, 1.6 W/cm$^2$). The increased temperature of mice were captured by an IR imaging device (FLIR ONE Gen3 IR imaging device (FLIR Systems, Arlington, VA, USA) every 1 min. Temperature changes were recorded using a visual IR thermometer (FLIR Tools).

### 2.20. In vivo anti-tumor efficacy

When the tumor size reached about 100 mm$^3$, 36 tumor-bearing mice were randomly divided into six groups ($n = 6$ per group). The mice were intravenously injected with 200 μL of saline (groups 1 and 2), FHP (HSA 300 μg/mL, Fe 500 μg/mL; groups 3 and 4), and FGP (GOx 300 μg/mL, Fe 500 μg/mL; groups 5 and 6). Groups 1, 3, and 5 were not treated any further. Groups 2, 4, and 6 additionally received NIR by irradiating the tumor region with 808 nm (1.6 W/cm$^2$) for 3 min 24-h post-injection. Tumor volumes and body weights of the mice were simultaneously recorded every 2 days. The tumor volume was calculated as Eq. (1):

$$\text{Tumor volume} = (\text{Width} \times \text{Width} \times \text{Length})/2 \quad (1)$$

On Day 15, the tumors were collected from anesthetized mice and each wound was carefully sutured. Each tumor was weighed. After 3 weeks, the mice were sacrificed and the lungs of each group were collected and rinsed with PBS. The metastatic nodules on the pulmonary tissues were counted, and the lung sections were stained by Hematoxylin and Eosin (H&E) to further evaluate the metastatic foci. To evaluate the therapeutic efficacy of the different treated groups, the tumor-bearing mice were treated as described about and tumors were removed on Day 4 for hematoxylin and eosin (H&E) and Ki67 staining and terminal deoxynucleotidyl transferase dUTP nick end labeling (TUNEL) analysis.

### 2.21. ICD amplifier to enhance anti-CTLA4 immunotherapy

Mice bearing both left and right 4T1 tumors were used to evaluate the therapeutic efficacy of FGP combined with anti-CTLA4 immunotherapy. To establish the bilateral tumor model, the right flank (primary tumor) was injected with $1 \times 10^6$ cells and the left

flank (distant tumor) was injected with $2 \times 10^5$ cells. After inoculation about 7 days, the primary tumor reached nearly 100 $mm^3$. The mice were divided into five groups ($n = 6$ per group). The groups received saline (group 1), saline + anti-CLTA4 (group 2), FHP (HSA 300 μg/mL, Fe 500 μg/mL)+ anti-CLTA4 (group 3), FGP (GOx 300 μg/mL, Fe 500 μg/mL) + anti-CLTA4 (group 4), and FGP + anti-CLTA4 (group 5). Groups 2, 3, and 5 additional were treated using NIR laser irradiation (808 nm, 1.6 W/$cm^2$) for 1 min and irradiated for 3 times (total 3 min), after 24-post injection. The interval between irradiations was 1min to avoid increased temperature of single NIR laser irradiation. The anti-CTLA4 antibody was intravenously injected about 20 μg per mouse on Days 2, 5 and 8. The primary and distant tumor growth curves were obtained within 14 days.

For CRT expression and DC maturation *in vivo*, the tumor-draining lymph nodes (TDLN) and primary tumors were collected on Day 3 after the various treatments as described above. Frozen sections of primary tumors in each group were stained with CRT primary antibody and fluorochrome-conjugated secondary antibody according to the standard protocols. They were also stained with DAPI. Finally, the fluorescence images were captured by fluorescence microscope. The TDLN were ground and filtered to obtain single cell suspensions. The cells were stained with FITC anti-mouse CD11c (Clone: N418, Catalog: 117,305), PE anti-mouse CD86 (Clone: GL-1, Catalog: 105,008) and APC anti-mouse CD80 (Clone: 16-10A1, Catalog: 104,714) antibodies (all from BioLegend, San Diego, CA, USA). The samples were examined by flow cytometry.

For the evaluation of T cell infiltration, distant tumors were collected on Day 7 after the different treatments. They were digested with an enzyme mixture and filtered to prepare single cell suspension. Then the cells were stained with APC anti-mouse CD3 (Clone: 17-A2, Catalog: 100,235; BioLegend) and PE anti-mouse CD8 (Clone: 53-6.7, Catalog: 100,708; BioLegend) antibodies and collected for flow cytometry analysis. The immunofluorescence staining of CD8 and IFN-γ was also performed in distant tumors. Images were captured by fluorescence microscopy (Nikon).

### 2.22. *Biosafety of FGP in vivo*

Six female ICR mice were randomly assigned to two groups for assessment of the blood glucose levels assessment ($n = 3$ per group). The mice were intravenously injected with saline and FGP (GOx 300 μg/mL, Fe 500 μg/mL). A commercial glucometer blood was employed for the detection of glucose in mice blood samples at the predesigned time interval (0, 1, 2, 3, 6, 9, 12 and 24 h) post injection.

The blood biochemical analyses of ALT, AST, ALP, BUN, and CREA were performed to indicate the biosafety of FGP. After treatment with FGP and saline for Days 1, 3, and 7, the whole blood was collected from these four groups and centrifuged, and the supernatant were analyzed. Organs were harvested and H&E staining was performed.

## 3. Results and discussion

### 3.1. *Preparation and characterization of FGP*

FGP nanoparticles were prepared by two steps *via* the hydrophobic drug-induced assembly method. First, ultrasmall FeS-GOx nanodots were synthesized by a facile enzyme-biomimetic route at room temperature[51]. And then, a clinically used paclitaxel chemotherapeutic drug was introduced to the co-assembled FeS-GOx nanodots by hydrophobic interaction to form larger FGP nanoparticles[52]. As evident in the representative TEM images in Fig. 2A and B, the synthesized FeS-GOx nanodots and FGP nanoparticles were uniform in size with the average diameter of 12 and 160 nm, respectively. These measurements were similar to the dimensions obtained by dynamic light scattering (DLS) (Fig. 2C). These results indicated the successful assembly of FeS-GOx nanodots to FGP mediated by PTX. In addition, in this study, PTX was used as model drug to induce the self-assemble of FeS-GOx. The other anti-inflammatory drugs or photosensitizes (such as curcumin, piperine and IR780) could also induce ultrasmall FeS-GOx nanodots to form larger nanoparticles (Supporting Information Fig. S1). The prepared FGP were stable in water and could be easily dispersed. Their particle size distribution and zeta potential showed no significant change within 48 h (Fig. 2D and Supporting Information Fig. S2). The UV−Vis-absorption spectra of FeS-GOx nanodots and FGP varied in the NIR absorption, which is suitable feature of photothermal agents (Fig. 2E).

As shown in Fig. 2F, the X-ray diffraction patterns (XRD) of FGP and GOx showed no crystalline peaks, indicating that the embedded FeS nanodots were in an amorphous phase. Energy-dispersive spectrometry (EDS) and X-ray photoelectron spectroscopy (XPS) were performed to confirm the structure and components of FGP. The FGP nanoparticles were confirmed to contain the C, O, Fe and S elements (Fig. 2G). In addition, the Fe and S elemental composition in FGP was further confirmed by scanning electron microscopy (SEM)-EDS mapping (Fig. 2H). XPS of FeS-GOx nanodots revealed a binding energy of 710.8 eV as characteristic peak of FeS, with Fe (2p1/2) binding energy of 724.5 eV (Fig. 2I)[43]. The concentration of $Fe^{2+}$ was determined by 2-2′ dipyridyl in a standard manner (Supporting Information Fig. S3) and the calculated FGP loading efficacy was 5.6%. The PTX and GOx contents in these nanoparticles were 45.8% and 32.5%, as determined by HPLC (Supporting Information Fig. S4) and BCA protein assay kit, respectively. These results indicated that FGP nanoparticles were successfully prepared by biomineralization and the drug-induced self-assembly method.

### 3.2. *Fenton reaction properties and PTT of FGP*

GOx is a catalyst that facilitates the reaction of glucose and oxygen to produce $H_2O_2$ and gluconic acid[53]. The oxygen consumption, $H_2O_2$ generation and pH decreased were monitored over time to evaluate the enzyme activities of FGP nanoparticles. As shown in Fig. 3A, rapid oxygen consumption was observed after with addition of glucose due to the catalytic activity of GOx in FGP. In addition, a significant pH decline from 7.2 to 3.0 was observed after the treatment of FGP with glucose for 90 min. The rate of decline of pH was related to the concentration of GOx (Fig. 3B). With oxygen consumption, $H_2O_2$ was generated as determined by a fluorimetric hydrogen peroxide assay. As shown in Fig. 3C, the concentration of $H_2O_2$ in FGP increased after addition of glucose. Interestingly, compared to the same concentration of free GOx (Supporting Information Fig. S5), $H_2O_2$ generation in FGP decreased after adding glucose for 15 min, which indicated that the $H_2O_2$ produced from the catalytic oxidation was consumed in Fenton reaction of FGP.

To confirm the ·OH generation, TMB oxidization and MB degradation of FGP with glucose were determined by examination

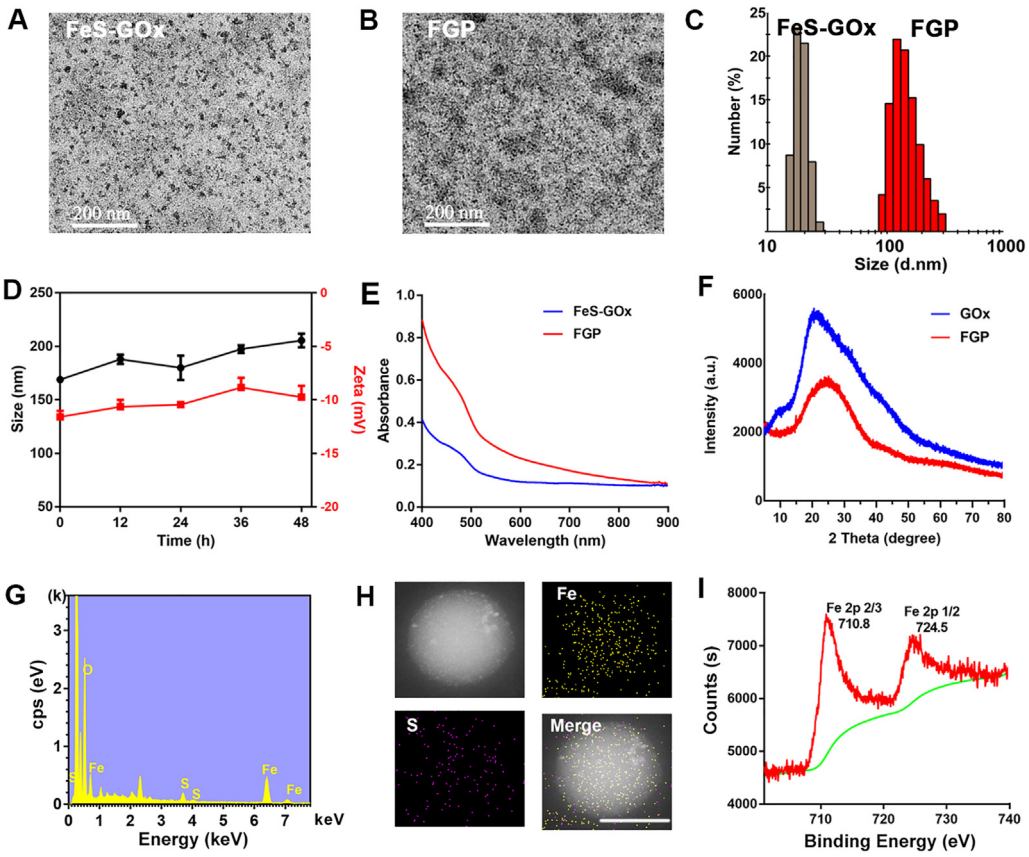


**Figure 2** Characterization of formed nanoparticles. (A, B) The TEM images of FeS-GOx and FGP. Scale bar = 200 nm. (C) Hydrodynamic size distribution of FeS-GOx and FGP by DLS. (D) Particle size and Zeta potential changes of FGP within 48 h in PBS. (Black and red line represent size and zeta potential, respectively). Data are presented as mean ± SD ($n$ = 3). (E) UV−Vis absorption spectra of FeS-GOx and FGP. (F) X-ray diffraction patterns (XRD) of FGP and GOx. (G) EDS spectrum of FGP. (H) The corresponding elemental mapping images of FGP. Scale bar = 200 μm. (I) High-resolution XPS spectrum of Fe 2p of FGP nanoparticles.

of the UV−Vis spectra. In the presence of ·OH, colorless TMB is oxidized to blue oxide of TMB, with a major absorbance peak at 652 nm[54]. As shown in Fig. 3D, a blue-colored solution with a unique absorption peak was obtained after treatment of FGP with a TMB-glucose solution. In addition, the degradation of MB over time is displayed in Fig. 3E. After 30 min, MB had almost completely degraded, confirming the production of ·OH by FGP and glucose. MB degradation was enhanced by the increased concentration of FGP due to the generation of more $H_2O_2$ (Supporting Information Fig. S6). On the basis of the above results, electron spin resonance (ESR) using DMPO was further performed to detect ·OH production capacity of FGP (Fig. 3F). A strong ESR signal of radical spin adduct was observed after mixing FGP with glucose. The other groups (glucose, FGP and FHP) did not show any significant spectra. These results confirmed that FGP could catalyze glucose to generate $H_2O_2$ and ·OH for starvation and chemodynamic therapy.

Taking hypoxia in deeper regions of a tumor into consideration, MB was used as an ·OH -specific indicator to evaluate the performance of the Fenton reaction of FGP nanoparticles under the hypoxic or normal condition. The hypoxic condition was created by continuing pump nitrogen into solution. Compared with FGP in the hypoxic condition, the MB absorbance of FGP in the normal condition was significantly decreased, indicating that hypoxia limited the ·OH generation of FGP (Fig. 3G). This may be because in the absence of oxygen, the enzyme catalytic activity could inhibit the oxidation of glucose to generate $H_2O_2$ and the Fenton reaction production of ·OH. These findings indicated that single chemodynamic therapy of FGP would not be a better treatment in cancer.

Due to the broad absorbance of FGP, the PTT effect was evaluated using 808 nm laser as the light source. As shown in Fig. 3H, the temperature of FGP at different concentrations was significantly increased under laser irradiation (808 nm, 1.8 W/cm$^2$, 5 min). The temperature of FGP increased approximately 21 °C at the Fe concentration of 600 μg/mL. Furthermore, this photothermal conversion effect was very stable during five cycles of irradiation (each cycle comprised 5 min irradiation with an intervening 5 min), as shown in Supporting Information Fig. S7. It has been reported that the PTT could enhance GOx activity and produce more $H_2O_2$ for the Fenton reaction. As shown in Supporting Information Figs. S8 and S9, with a temperature increase from 30 to 55 °C, the $H_2O_2$ was significantly increased, and pH decreased more quickly. These results indicated that the PTT effect of FGP could enhance GOx activity. Thus, the efficiency of ·OH production was then examined to understand the promoting role of PTT. The MB decoloration experiment clearly demonstrated that the heat generated from the photothermal conversion could accelerate and improve ·OH generation (Fig. 3I). This was because the increased temperature simultaneously promoted the activity of GOx. The collective results confirmed that FGP could

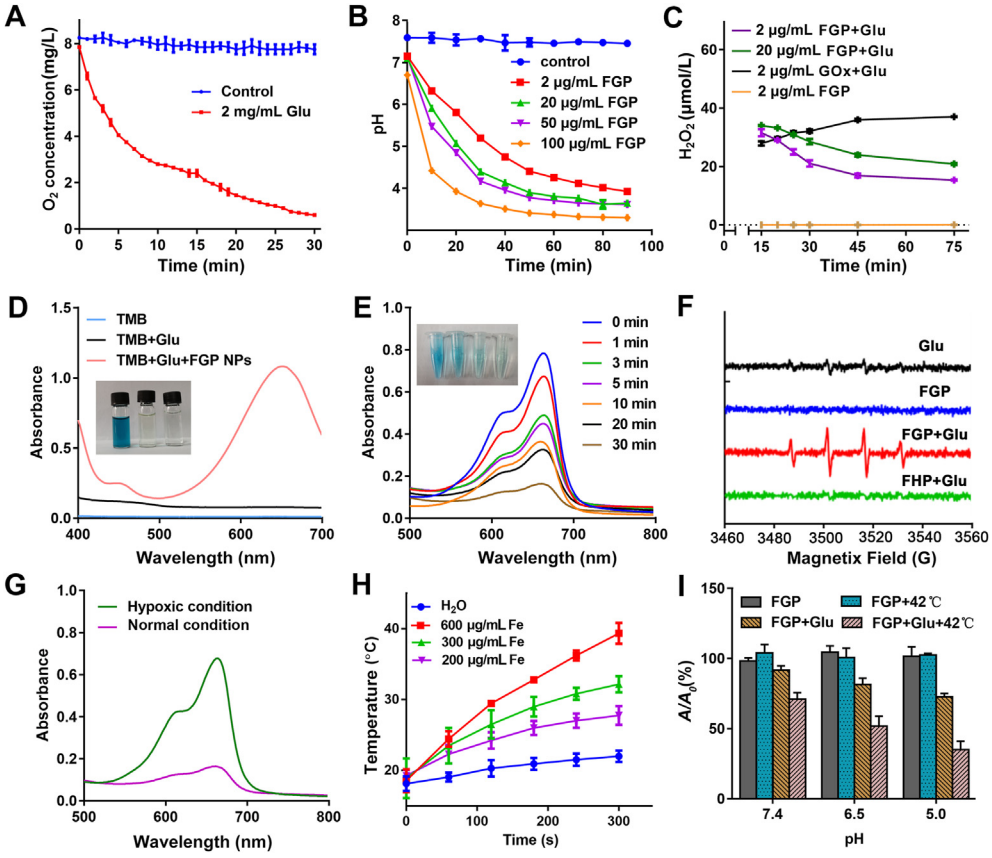


**Figure 3** Intrinsic properties of FGP nanoparticles. (A) Oxygen consumption of FGP (GOx, 2 μg/mL) with addition of glucose. (B, C) The variation of time-dependent of pH changes and $H_2O_2$ generation of FGP with glucose (2 mg/mL). (D) TMB was oxidized by ·OH to blue oxide of TMB (oxTMB). The UV−Vis absorption spectra of TMB with addition of FGP and glucose (10 mg/mL). (E) Time-course absorbance of MB degradation of FGP (GOx, 200 μg/mL) with glucose (10 mg/mL). (F) Colorimetric analysis of the Fenton reaction for MB decolorization of FGP with glucose under hypoxic and normal conditions. (G) ESR spectra of different groups (GOx, 200 μg/mL) upon the addition of DMPO (trapping agent of ·OH). (H) Temperature curve at varied concentrations of Fe in FGP nanoparticles. (I) The MB degradation of FGP (GOx, 200 μg/mL) with glucose (4 mg/mL) in different pH and temperature conditions. Data are presented as mean ± SD ($n$ = 3).

accelerate ·OH by PTT and the benefit of the combined PTT, amplified chemodynamic and starvation therapy for cancer treatment.

### 3.3. *Fenton reaction of FGP in tumor cells*

To better evaluate the Fenton reaction of FGP for cancer cell treatment, Ce6-labeled FGP was incubated with 4T1 cells for 0.5, 1 and 2 h, and the cellular uptake was studied by flow cytometry analysis. As observed in Supporting Information Fig. S10, the amount of FGP at the cellular level increased significantly with time. As confirmed above, GOx was the key point in FGP to catalyze glucose to produce $H_2O_2$ and ·OH for starvation and chemodynamic therapy. Cellular cytotoxicity was evaluated in 4T1 cells by the CCK-8 assay. As shown in Fig. 4A, treatment of FHP with glucose and FGP treatment without glucose were less toxic to cancer cells. In the case of the same concentration of GOx and glucose, FGP was significantly toxic to normoxic cancer cells compared to hypoxic cancer cells. These results indicated that GOx in FGP could consume glucose with oxygen to generate $H_2O_2$ and induce the Fenton reaction, thus killing cancer cells. To confirm the mechanism of cytotoxicity in 4T1 cells, the generated ROS were stained with the DCFH-DA fluorescence probe. As revealed in Fig. 4B, cells treated with FGP showed slight green fluorescence of DCFH compared to cells treated with FHP. The findings suggested that GOx could effectively catalyze the glucose into $H_2O_2$ and generate ·OH. Week fluorescence was also observed in 4T1 cells treated with FHP, probably due to the endogenous $H_2O_2$ of tumor cells and the slight amount of ·OH produced by endogenous $H_2O_2$ in the Fenton reaction. The trends observed after DCF staining were further validated by quantitative flow cytometric analysis (Fig. 4C).

The cellular generation of $H_2O_2$ in 4T1 cells was determined by a fluorimetric hydrogen peroxide assay after incubation with different concentrations of FGP. As showed in Fig. 4D and Supporting Information Fig. S11, compared with the control group, the $H_2O_2$ generation in the FGP groups was significantly increased and a similar decreasing trend was observed in FGP groups after incubation for approximately 30 min. The level of $H_2O_2$ initially increased and then decreased along with the catalytic oxidation and Fenton reaction.

To further confirm the ·OH generation of the Fenton reaction of FGP, the HPF commercial ·OH-specific fluorescent probe was applied to distinguish ·OH from $H_2O_2$ produced by GOx and to determine the intracellular ·OH (Fig. 4E and F). Compared to FHP treatment, cells treated with FGP showed slightly increased (2.6-fold) green fluorescence of HPF. This may be because FGP could speed up the oxidation of GOx to furnish excess $H_2O_2$ and generate more ·OH radicals. As known to us, $Fe^{2+}$ was the key point for Fenton reaction. So, the intracellular $Fe^{2+}$ was evaluated

by FerroOrange (Ex/Em = 490/515 nm), which is a novel fluorescent probe that enables live-cell fluorescent imaging of intracellular $Fe^{2+}$. As shown in Supporting Information Fig. S12, after incubation of FGP in 4T1 cells, the red fluorescence of $Fe^{2+}$ was brightly than that in control group, nearly 10-times. The control group also showed slight fluorescence due to the metabolism of iron in 4T1 cells. These results indicated that FGP nanoparticles could provide $Fe^{2+}$ to increase Fenton reaction for CDT treatment.

To accurately analyzed the viability of treated 4T1 cells, Annexin V-FITC and PI staining assay was performed by flow cytometric analysis (Fig. 4G and Supporting Information Fig. S13). The proportion of apoptosis cells was 44.37% after treatment with FGP and glucose, indicating that GOx-based starvation therapy and Fenton reaction could led to apoptosis of cancer cells. The results were also potential confirmation that the single treatment of FGP might not achieve better cancer treatment in the deeper hypoxic regions of tumors. Rather, FGP should be combined with PTT for cancer treatment.

### 3.4. *In vitro combination therapy of FGP to increase CRT expression*

Due to the increased temperature induced by the photothermal effect of FGP, the synergistic effect of starvation therapy, chemodynamic therapy and PTT was evaluated in 4T1 tumor cells in the presence or absence of NIR laser by CCK-8 assays. As demonstrated in Fig. 5A, compared with FHP treatment, a gradual decrease in the cellular viability of 4T1 cells was observed with increased concentration of GOx in FGP without laser irradiation. This may have reflected the efficacy of starvation and Fenton reaction. After NIR laser irradiation, both FHP and FGP showed increased cytotoxicity due to the photothermal effect of the FeS-GOx nanodots. To further evaluate the combination therapy of FGP, 4T1 tumor cells were stained with calcein-AM (green fluorescence) and PI (red fluorescence) to visualize live and dead cells, respectively. As illustrated in Fig. 5B and 4T1 cells that were not irradiated displayed higher red fluorescence when treated with FGP as compared to treatment with FHP. Under laser irradiation, the red fluorescence was increased in nearly 80% of cells, similar as the results determined by CCK-8 assays. In addition, Annexin V-FITC and PI staining assay was performed by flow cytometric analysis to confirm the therapeutic efficacy. As shown in Fig. 5C and Supporting Information Fig. S14, the proportion of apoptotic cells in the FGP treated group reached nearly 80%, which was 2-fold higher than that of the FHP treated group. The collective results indicated better therapeutic efficacy of FGP *in vitro*, due to the combination therapy of starvation, chemodynamic, and PTT.

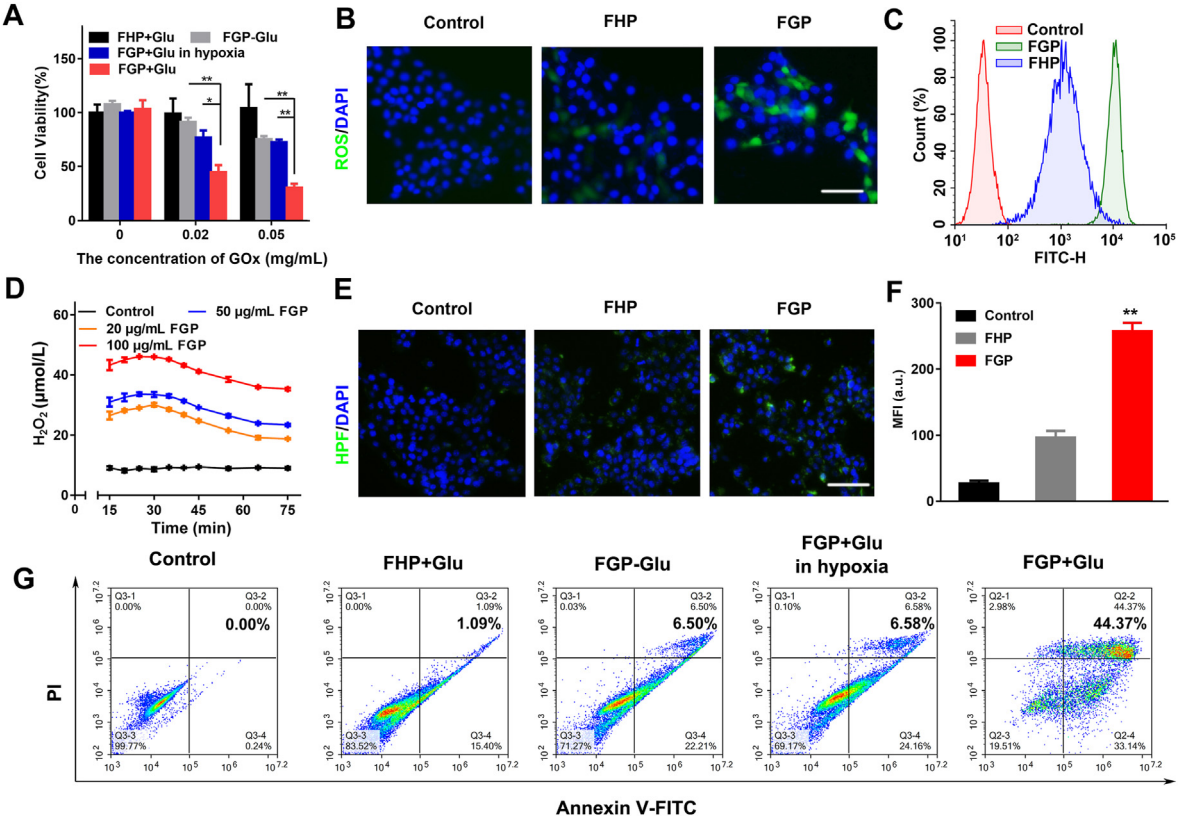


**Figure 4** Characterization of Fenton reaction of FGP nanoparticles at the cellular level. (A) Cell viability of 4T1 cells treated with various concentrations of FGP and FHP with or without glucose (2 mg/mL) in different conditions (hypoxia and normal). Statical significance was caculated by *t*-test. $^*P < 0.05$, $^{**}P < 0.01$. (B) Representative fluorescence images of 4T1 cells stained with H²DCFDA (Green) and DAPI (Blue) in different groups (Control, FHP and FGP) with glucose (2 mg/mL). Scale bar = 100 μm. (C) Flow cytometry quantitative analysis of ROS generation in treated groups. (D) The cellular $H_2O_2$ generation treated with various concentrations of FGP. (E, F) Representative CLSM images and semi-quantitative analysis of ·OH (Green fluorescence, stained with HPF). Data are presented as mean ± SD ($n = 3$, $^{**}P < 0.01$ FGP *vs.* other treatments). Scale bar = 200 μm. (G) Flow cytometry apoptosis of 4T1 cells treated with different groups stained by Annexin V-FITC and PI.

The photothermal effect and ROS generation reportedly enhance immunotherapy-related ICD, especially increased calreticulin (CRT) exposure on the surface of dying tumor cells[55]. As described above, FGP showed better synergistic therapeutic efficacy of cancer cells *in vitro*. CRT expression was explored by staining with CRT primary anti-body and Cy3-conjugated secondary antibody. The resulting green fluorescence was captured by CLSM. As shown in Fig. 5D and E, 4T1 cells treated with FGP and laser irradiated showed brighter green fluorescence (mean fluorescence intensity [MFI] of 179.3), which was nearly 4.1-fold higher than that of cells treated with FGP but without laser irradiation (MFI of 43.7). In addition, upon laser irradiation, the FHP group displayed more green fluorescence than that of cells treated with FGP and FHP but not laser irradiated (MFI of 58.2 *vs.* 22.6). These results indicated that combination therapy could increase CRT exposure of 4T1 cells.

As known to us, HMGB-1 released from dying cells could induce inflammation to attract immune cells and mature DC cells. So, the extracellular HMGB-1 was determined to evaluate ICD expression after different treatments in 4T1 cells. As show in Supporting Information Fig. S15, after treated with FHP and FGP without NIR irradiation, HMGB-1 was significantly increased due to the generation of ·OH. Furthermore, because of GOx catalyzed to increase $H_2O_2$ generation and induce more ROS, FGP showed

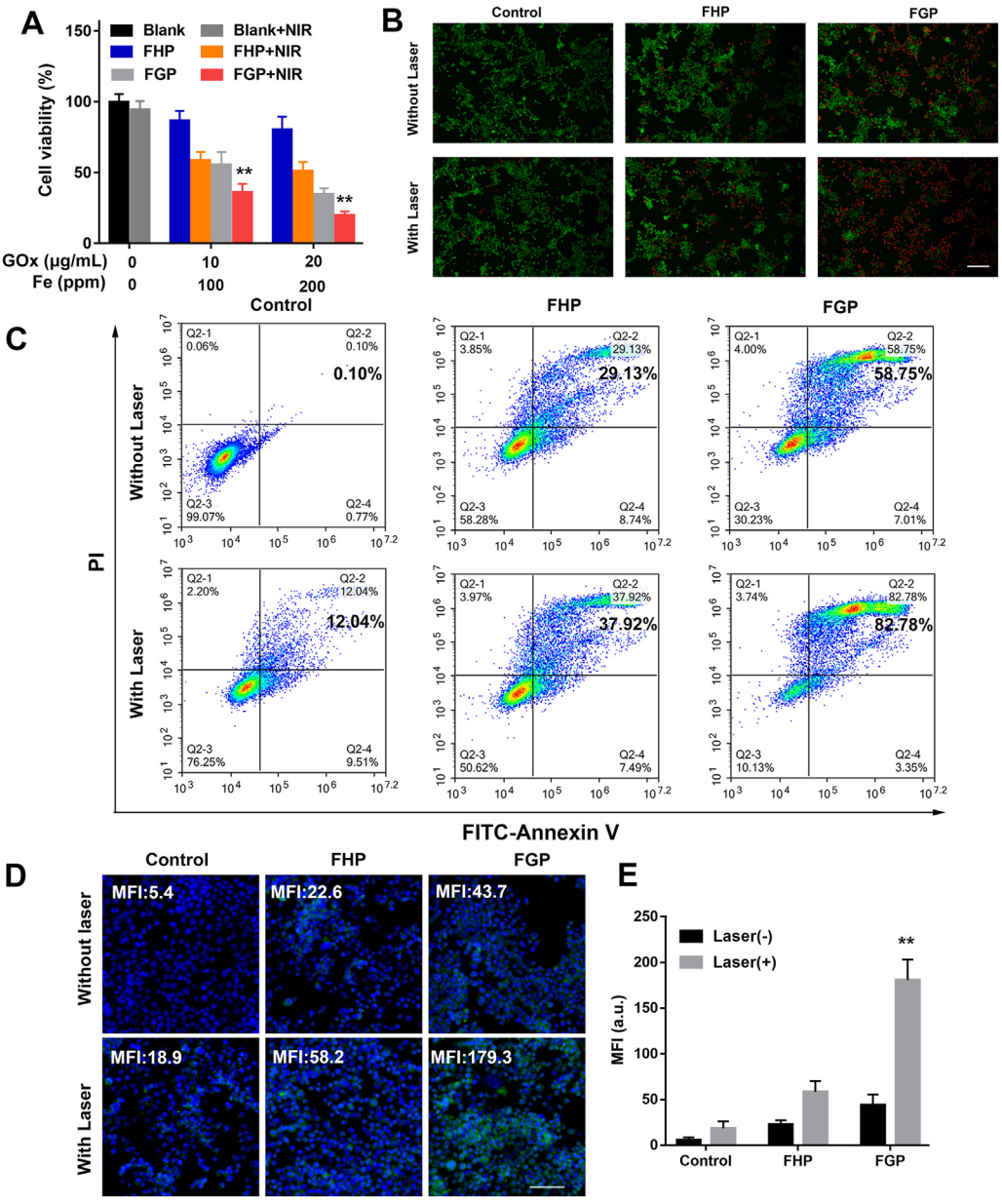


**Figure 5** *In vitro* cytotoxicity of FGP combined Fenton reaction with PTT. (A) Cell viability of 4T1 cells treated with various concentrations of FGP and FHP with or without NIR irradiation (808 nm, 1.6 W/cm$^2$). (B) Representative fluorescence images of dead and live 4T1 cells stained with calcein-AM (Green) and PI (Red) in different groups. Scale bar = 200 μm. (C) Flow cytometry apoptosis of 4T1 cells treated with different groups stained by Annexin V-FITC and PI. (D) and (E) CLSM images and semiquantitative analysis of CRT exposure on 4T1 cells surface treated with different groups. Scale bar = 200 μm. Data are presented as mean ± SD ($n$ = 3, $^{**}P < 0.01$ FGP with NIR *vs.* other treatments).

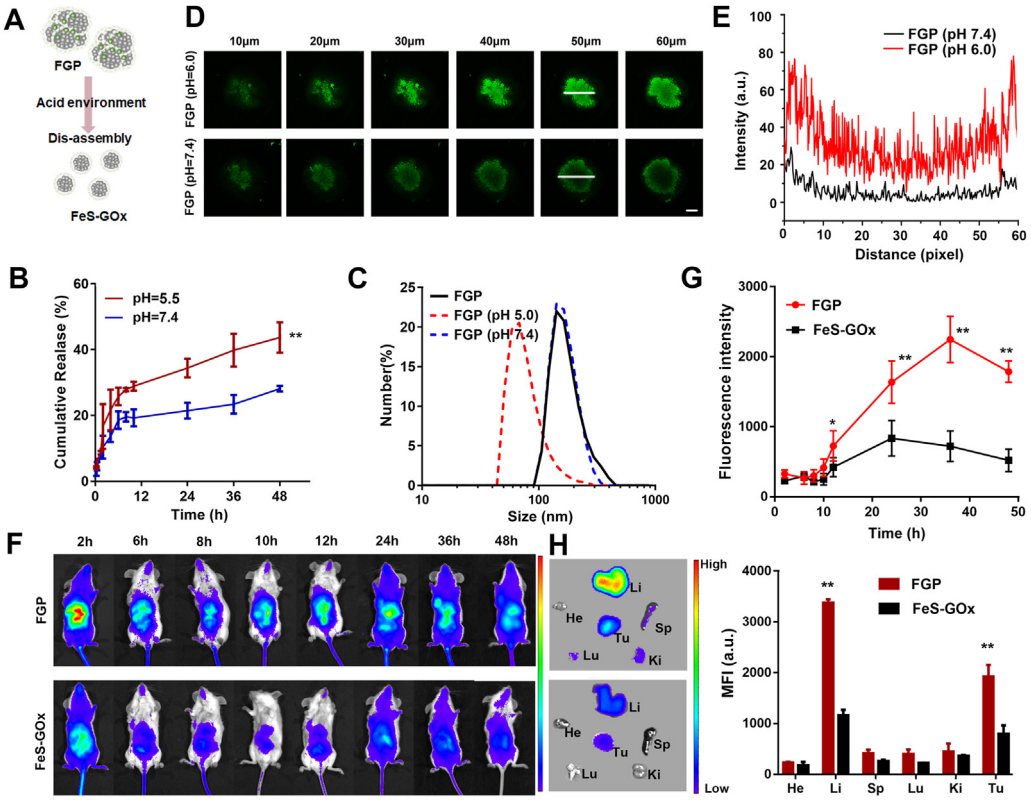


**Figure 6** The disassembly of FGP for tumor penetration. (A) Illustration of disassembly of FGP to form smaller nanoparticles with acid environment. (B) The release profile of PTX in FGP in different pH (5.0 and 7.4). Data are presented as mean ± SD ($n = 3$, $^{**}P < 0.01$, pH 5.5 *vs.* pH 7.4). (C) The size distribution of FGP cultured with pH 7.4 and pH 5.0 buffer within 12 h. (D) Tumor penetration of FGP incubated with pH 7.4 and pH 6.0 buffer on 4T1 3D cells (0−60 μm) observed by CLSM z-stack. Scale bar = 500 μm. (E) Dynamic Ce6 fluorescence intensity profiles of section labeled with white arrows in tumor cell spheroids at 50 μm. (F) and (G) The *in vivo* distribution of Ce6-FGP and FeS-GOx at different time points in 4T1 tumor-bearing mice. (H) *Ex vivo* fluorescence images and semiquantitative analysis of major organs and tumors at 48 h. Data are presented as mean ± SD ($n = 3$, $^{**}P < 0.01$, FGP *vs.* FeS-GOx).

significantly increased translocation of HMGB-1 from nuclear to extracellular medium, compared with FHP. After NIR laser irradiation, extracellular HMGB-1 of 4T1 cells in FGP was highest compared with other treatments. These results indicated that the designed FGP nanoparticles could release HMGB-1 from cancer cells and induce ICD to active immune response. In addition, the release of ATP in different treatments were also determined by bioluminescence assays. As shown in Supporting Information Fig. S16, compared with control groups, FHP and FGP with or without laser irradiation released more ATP to extracellular medium to active immune response, which is similar as the results of HMGB-1 and CRT expression. But the release of ATP in FGP (with or without laser) was lower than that in FHP group. This may be due to the catalyze property of GOx in FGP nanoparticles to consume glucose and decrease ATP generation in cancer cells as starvation therapy. But taking all the results of CRT expression, the release of ATP and HMGB-1 into consideration, FGP with NIR laser irradiation could amplify ICD to induce anti-tumor immune response.

### 3.5. *Disassembly of FGP for tumor penetration*

Previous studies reported that PTX induced self-assembly of nanoparticles and the release of PTX disassembled smaller nanodots[50]. The scheme showed the dissociation behavior of FGP, as illustrated in Fig. 6A. The release behavior of PTX from FGP at 37 °C was determined by HPLC. Approximately 43.6% of PTX was released at pH 5.5 within 48 h, was nearly 2-fold higher than that occurring at pH 7.4, indicating a pH-responsive release property of PTX (Fig. 6B). To confirm the pH-responsive degradability of the FGP, the particle size distribution of FGP was also determined at different PBS buffers (pH 7.4 and pH 5.0). After 24 h, no significant change of FGP was evident at pH 7.4, while smaller nanodots of approximately 30 nm were observed at pH 5.0 (Fig. 6C). These results indicated that the acid tumor microenvironment could rapidly induce FGP disassembly to release PTX and smaller FeS nanodots.

As the smaller nanodots could penetrate deeper into tumors, we were interested in evaluating whether the disassembly of FGP could promote tumor penetration *in vitro*. Ce6-labeled FGP nanoparticles were incubated with 4T1 multicellular tumor spheroids (MCTS) in culture medium with a pH of 7.4 or pH 6.0 cell for 24 h. MCTS incubated with FGP at pH 6.0 displayed strong Ce6 fluorescence in sections the 10−60 μm in thickness (Fig. 6D and E). In contrast, MCTS incubated with FGP at pH 7.4 displayed green fluorescence only at the margin regions of the 60 μm-thick sections, due to the limited penetration of the larger FGP. Taken together, the collective findings indicate that FGP could quickly disassemble to smaller FeS nanodots in acid tumor microenvironment and effectively penetrate into deep tumor.

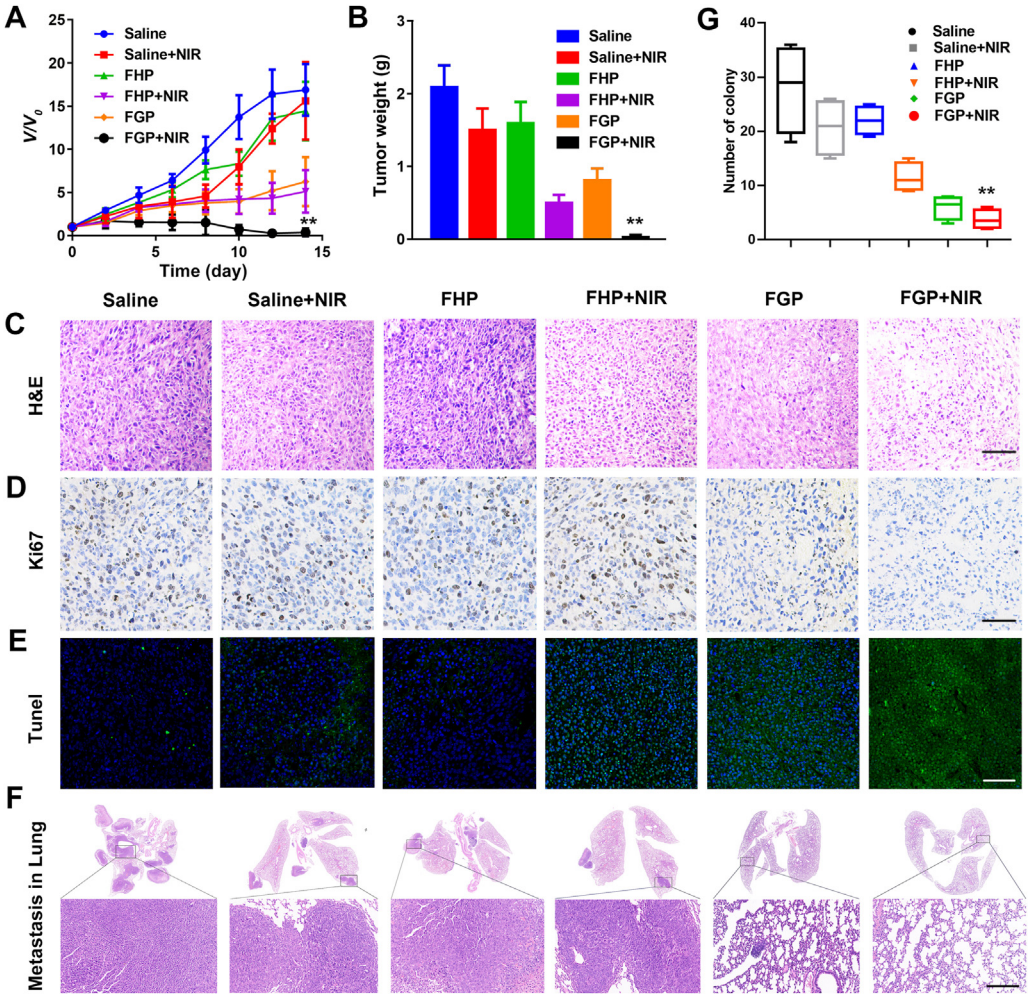


**Figure 7** *In vivo* antitumor and antimetastatic studies of FGP nanoparticles. (A) The relative tumor growth curves of 4T1 tumor-bearing mice after various treatments for 14 d. (B) The average tumor weight in each treatment at 14 d. (C–E) H&E staining, Ki67 immunohistochemical staining and TUNEL analysis of tumor tissues after different treatments. Scale bar = 200 μm. (F) The number of nodules on the surface of lung excised from 4T1 tumor-bearing mice. Scale bar = 500 μm. (G) Representative H&E staining of lungs. Data are presented as mean ± SD ($n = 6$,$^{**}P < 0.01$ FGP with NIR *vs.* other treatments).

The smaller FeS-GOx nanodots could enhance tumor penetration, but could be easily cleared out, leading to reduced tumor accumulation, due to the short circulation time[56]. Self-assembly FGP would maintain a relative larger size in blood and accumulate in tumor *via* EPR effect. Thus, the *in vivo* comparison of the tumor accumulation of Ce6-labeled FeS-GOx and FGP was conducted by near-infrared fluorescence (NIRF) imaging *in vivo*. As shown Fig. 6F and G, the intratumoral accumulation of FGP was enhanced with increased time and achieved maxima at 24 h post-injection. By contrast, 4T1 tumor-bearing mice treated with FeS-GOx showed weaker fluorescence signals than mice treated with FGP. The signals decreased rapidly, probably due to rapid clearance of small FeS-GOx in the physiological environment. At 48 h post-injection, mice were euthanized, and the major organs and tumors were dissected for *ex vivo* biodistribution analyses (Fig. 6H). Strong fluorescence signals and relatively high MFI were found in the tumors of mice treated with FGP, while weak fluorescence was observed in FeS-GOx treated mice. These results showed that FGP could accumulate in tumor for cancer therapy. In addition, as shown in Supporting Information Fig. S17, after intravenous injection of FGP, the red fluorescence of Ce6-labeled FGP was observed in all tumors frozen slice. Furthermore, the fluorescence of Ce6 was also observed in tumor cells, which indicated that nanoparticles could access into cancer cells, which is possible to induce ICD after treatment of FGP. The concentration of $Fe^{2+}$ in tumor was also evaluated by corresponding Iron assay kits (Dojindo), after intravenous injection of saline and FGP. As shown in Supporting Information Fig. S18, the concentration of $Fe^{2+}$ was higher than that in saline group. These results further indicated that FGP could accumulate and enhance tumor penetration at tumor site. The collective data indicated that the large size of FGP nanoparticles could enhance accumulation at tumors with subsequent disassemble to smaller nanodots allowing deeper penetration.

### 3.6. *In vivo anti-tumor and anti-metastatic effect of FGP*

FGP along with NIR laser irradiation can effectively increase temperature in cancer treatment. As shown in Supporting Information Figs. S19 and S20, after 24 h-post injection of FGP and FHP,

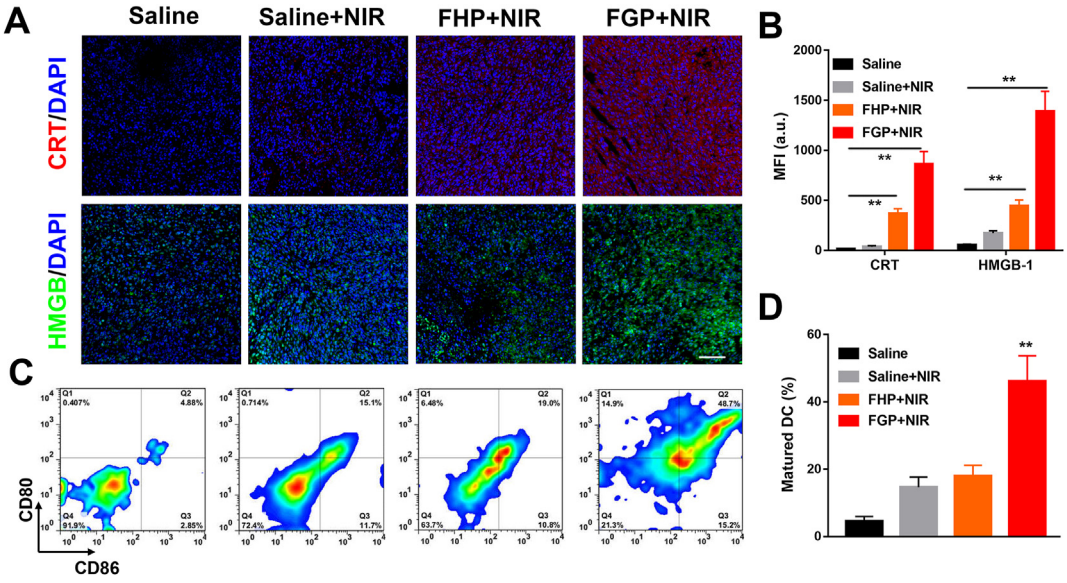


**Figure 8** Amplification of ICD to promote DC maturation *in vivo*. (A) Immunofluorescence staining and (B) fluorescence intensity calculated based on examination of sections by Image J software of CRT and HMGB-1 in tumors of mice with different treatments ($n \geq 10$, $^{**}P < 0.01$). Scale bar = 100 μm. (C) Representative flow cytometry analysis images and (D) relative quantification of DC maturation ($CD11c^{+}CD86^{+}CD80^{+}$) in LNs after various treatments *in vivo*. Data are presented as mean ± SD ($n = 6$, $^{**}P < 0.01$, FGP with NIR *vs.* other treatments).

infrared thermal images and temperature curves showed that the temperature was quickly increased and reached about 58.7 °C, with no significance between the FHP and FGP groups, due to the equal concentration of FeS. In addition, the therapeutic efficacy of tumor inhibition of FGP was evaluated in 4T1 tumor-bearing mice. After the tumor reached a volume of approximately 100 $mm^3$, the tumor-bearing mice were divided to six groups, including saline, FHP, and FGP with or without NIR laser irradiation. The relative tumor volumes presented in Fig. 7A demonstrated that saline with NIR and FHP showed some degree cancer inhibition in the first days after treatment due to the increased temperature or Fenton reaction. However, thereafter tumors grew quickly and there was no significant different with the control group. In addition, due to the photothermal effect of FHP and starvation, and the Fenton reaction of FGP, mice in both two groups treated with FHP plus NIR and FGP showed an approximately 60% rate of tumor inhibition. However, the tumor growth in mice treated with FGP plus NIR was significantly suppressed and was almost eliminated. Tumor weight was consistent with the results of relative tumor volumes (Fig. 7B and Supporting Information Fig. S21). These results indicated that the combination therapy of FGP could effectively inhibit tumor growth due to the higher accumulation and deep penetration *in vivo*.

The therapeutic efficacy of different treatments was further evaluated by H&E staining and TUNEL assay. As shown in Fig. 7C, extensive cell damage was observed in the group treated with FGP plus NIR laser irradiation, consistent with the results of TUNEL staining (Fig. 7E). Nearly all tumor cells were dead following the synergistic therapy of FGP and NIR irradiation. In addition, immunohistochemical staining of tumor sections for Ki-67 antigen was employed to determine the extent of tumor cell proliferation (Fig. 7D). Visually, tumor cells in the FGP plus NIR group exhibited decreased Ki-67 expression indicating markedly reduced tumor cell proliferation and tumor metastasis after treatment. The number of pulmonary metastatic nodules was quantified to further evaluate the anti-metastasis efficacy after tumor treatment. As shown Fig. 7F, H&E staining of lung tissue slices revealed the pronounced presence of metastatic nodules in saline group, while lung metastasis was negligible in mice treated with FGP plus NIR irradiation. In addition, the groups treated with FHP plus NIR irradiation and FGP displayed a decreased number of metastatic nodules (Fig. 7G). The collective results indicated that the combination therapy of FGP could enhance antitumor efficacy and inhibit tumor metastasis.

### 3.7. *Biosafety evaluation of FGP*

Biological safety was evaluated according to the weight of mice after different treatments. There showed no significant difference between these groups, indicating that FGP had no obvious toxicity for mice (Supporting Information Fig. S22). Also, the major organs were harvested and stained with H&E. No distinct tissue damage was observed (Supporting Information Fig. S23). Given the prior demonstration that GOx in FGP catalyzed the reduction in level of glucose, the blood glucose was determined after intravenous injection of FGP. Compared with the saline group, the blood glucose was slightly decreased in the first few hours, and quickly recovered to the level of the saline group (Supporting Information Fig. S24). In addition, there were no obvious changes in the levels of AST, ALT, ALP and CREA in the FGP treated group, which indicated that FGP was safe for the liver and kidney (Supporting Information Figs. S25 and S26). The hematology marker of FGP treatment did not change on Days 1, 3 and 7 (Supporting Information Fig. S27). All these results demonstrated that the safety of FGP for cancer treatment *in vivo*.

### 3.8. *In vivo CRT expression and DC maturation*

Foregoing results proved that the combination therapy of FGP could boost the ICD of 4T1 cell *in vitro*. To verify whether the significant tumor inhibition benefited from an ICD induced

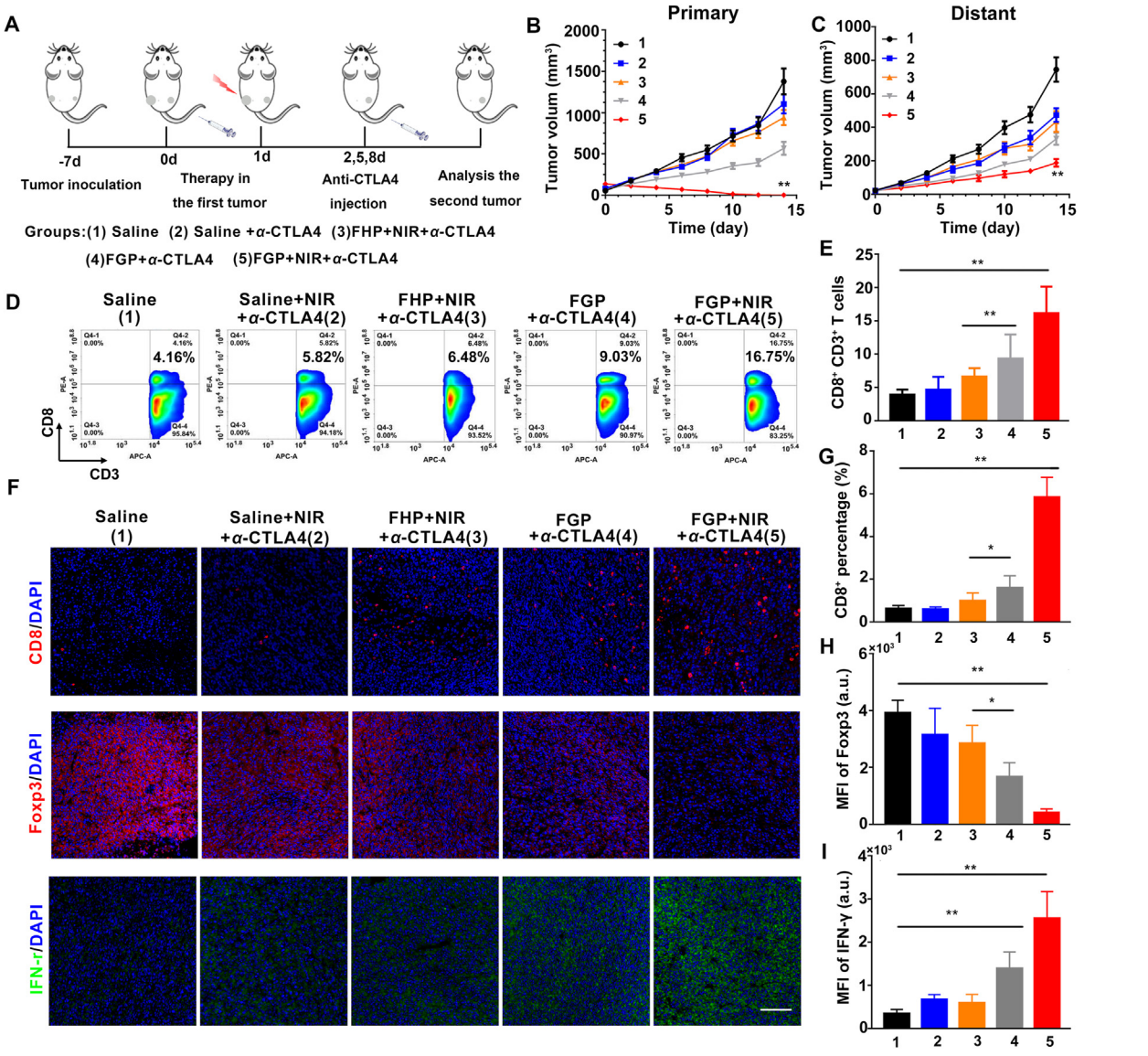


**Figure 9** Antitumor immune effect of FGP combined with ICB immunotherapy. (A) Schematic illustration of combining FGP with α-CTLA4 therapy to inhibit tumor growth at primary or distant sites (1. Saline, 2. Saline with α-CTLA4, 3. FHP with NIR laser and α-CTLA4, 4. FGP with α-CTLA4, 5. FGP with NIR laser and α-CTLA4). (B) Primary and (C) distant tumor growth curves of 4T1-bearing mice after various treatments. Data are presented as mean ± SD ($n = 6$, $^{**}P < 0.01$, FGP with NIR and α-CTLA4 *vs.* other treatments). (D) Representative flow cytometric analysis images and (E) relative quantification of CD8+T cells gating on CD3+ cells. (F) Representative immunofluorescence images of tumor slices from distant tumors of mice with various treatments. The slices were stained with anti-CD8, anti-Foxp3 and anti-IFN-γ antibody. Scale bar = 200 μm. Statistical analysis of (G) CD8+T cells, (H) positive Foxp3 and (I) IFN-γ fluorescence in tumor slices, which was calculated by Image J software. Data are presented as mean ± SD ($n \geq 10$, $^{*}P < 0.05$, $^{**}P < 0.01$, two-side Student's *t*-test).

immune effect, the ICD markers of CRT and HMGB-1 expression were also evaluated *in vivo* following various treatments of mice[57]. As shown in Fig. 8A and B, bright fluorescence was observed in tumors treated with FHP and NIR irradiated compared with the control group, indicating that PTT could induce ICD of tumor cells. Of note, the synergistic therapy of FGP remarkably induced CRT translocation and HMGB-1 expression by nearly 3-fold compared to the observations following FHP plus NIR irradiation, highlighting that the increased ROS generation and photothermal effect of FGP could amplify ICD to provoke an antitumor immune response. Given the satisfactory ICD-induction of FGP, the maturation of DC ($CD11c^{+}CD80^{+}CD86^{+}$) in lymph nodes (LNs) was analyzed by flow cytometry after various treatments on Day 3. The percentage of matured DCs increased significantly in the FGP plus PTT group compared with saline group (48.7% *vs.* 4.88%). The increase was much higher than that in the saline plus NIR irradiation group (15.1%) and FHP plus NIR irradiation group (19.0%) group (Fig. 8C and D). These results indicated that the FGP treatment could efficiently promote DC maturation by boosting the ICD of tumor cells.

### 3.9. *In vivo combination therapy of FGP and ICB immunotherapy*

The demonstration that FGP could increase CRT expression to amplify ICD and promote DC maturation indicated that FGP

might induce tumor-specific immune response to attack cancer cells. We evaluated the immune therapeutic efficacy of the combination of FGP and CTLA-4 blockade therapy to destroy local tumors and eliminate distant metastatic tumors. As illustrated in Fig. 9A, each mouse was subcutaneously inoculated with two CT26 colorectal tumors on both flanks. The tumor in the left flank (the primary tumor) was treated by FGP with NIR laser irradiation. The distant tumor in right flank was designed as the model of abscopal tumor. Then, the mice were divided randomly into five groups, including: (1) Saline, (2) Saline + NIR+$\alpha$-CTLA4, (3) FHP + NIR+$\alpha$-CTLA4, (4) FGP+$\alpha$-CTLA4, (5) FGP + NIR+$\alpha$-CTLA4. After 24 h following intravenous injection, NIR laser irradiation (808 nm, 1.8 W/cm$^2$) was performed only on the primary tumors. Afterward, CTLA4 blockade therapy was adopted three times by the intravenous injection of anti-CTLA4 at the dosage of 10 μg per mouse on Days 2, 5 and 8.

The tumor growth curves of the primary tumors and distant tumors were monitored every second day to assess the therapeutic effect. As expected, the FGP plus NIR group exhibited a near complete inhibition of primary tumor growth (Fig. 9B). Most notably, for tumors at the left side (distant tumor) without NIR treatment, the FGP + NIR group also induced the most pronounced tumor growth inhibition among all five groups (Fig. 9C). These results indicated that the combination therapy of FGP with CTLA4 blockade could enhance immunotherapy to inhibit distant metastatic tumors, due to the amplified ICD of FGP. It has been well-known that cytotoxic T lymphocytes (CTLs) play a positive role in cancer immunotherapy. To understand the mechanism underlying the inhibition of distant tumors after combination therapy, the CTLs were analyzed in the untreated distant tumors on Day 8 after the different treatments in primary tumor. As displayed in the flow cytometry analysis (Fig. 9D and E), the percentage of CTLs ($CD3^+CD8^+$) that could directly kill targeted tumor cells manifestly increased to 16.75% in the group treated with FGP plus NIR, which was 4.1 times higher than that of the saline group (4.16%). The levels of $CD8^+$ T cells, $Foxp3^+$ cells and IFN-$\gamma$ in distant tumors were further analyzed by immunofluorescence staining (Fig. 9F). It was found the FGP and FHP plus NIR showed slightly fluorescence increased, while enhanced percentage of $CD8^+$ T cells (Fig. 9G) and fluorescence intensity of IFN-$\gamma$ (Fig. 9I) were observed in FGP plus NIR irradiation combined with $\alpha$-CTLA4. These results may have reflected the strong immune activation of FGP treatment. It is well known that antitumor immunotherapy is suppressed by regulatory T cells (Treg, $Foxp3^+$). The levels of Foxp3-positive Treg cells decreased in distant tumors of FGP plus NIR irradiation and CTLA4 blockade groups (Fig. 9H). The collective results demonstrated that the amplified ICD induced by the synergistic therapy of FGP produced a strong anti-tumor immunotherapy to inhibit distant tumors.

## 4. Conclusions

In summary, a cascade bioreactor was successfully developed that involved the PTX induced self-assembly of FeS-GOx nanodots *via* hydrophobic interaction. Due to the mild biomineralization method, FGP maintained high enzymatic activity of GOx to consume glucose and generate $H_2O_2$, and thereby producing more ·OH for CDT enhancement. Due to the acid tumor microenvironment, FGP could quickly disassemble to release ultrasmall FeS-GOx with enhanced tumor penetration in 3D tumor spheroids. With NIR laser irradiation, the photothermal effect induced a temperature increase that significantly promote GOx activity. In addition, the combination therapy of FGP could effectively kill tumor cells and increase CRT exposure in dying tumor cells to amplify ICD both *in vitro* and *in vivo*. The amplified ICD with CRT and HMGB-1 expression promoted antigen presentation and maturation of DCs to strengthen anti-tumor response. In combination with anti-CTLA4 blockade therapy, increased infiltration of CTLs was observed in distant tumors after treated with FGP bioreactor. The synergetic therapy of FGP could completely eliminate tumors and significantly suppress distant tumors with enhanced activation of anti-tumor immune response. Therefore, this work provides a promising strategy of the simply constructed and synergistic comprehensive cancer therapy, which can eliminate primary tumors and enhance the immune response for the inhibition of metastasis.

## Acknowledgments

This work was financially supported by the Youth Foundation of Jiangsu province (No. BK20180699, China), National Natural Science Foundation of China (Nos. 81803439, and 81703940).

## Author contributions

Hao Ren, Xueming Li and Jiahui Yong designed the research. Jiahui Yong carried out the experiments and performed data analysis. Qingqing Yang, Zhen Yang, Zhangya Liu, Yan Xu and Hao Wang participated part of the experiments. Hao Ren and Jiahui Yong wrote the manuscript. Xing Jiang, Hao Ren and Wenjun Miao revised the manuscript. All of the authors have read and approved the final manuscript.

## Conflicts of interest

The authors have no conflicts of interest to declare.

## Appendix A. Supporting information

Supporting data to this article can be found online at https://doi.org/10.1016/j.apsb.2021.05.005.

## References

1. Topalian SL, Taube JM, Anders RA, Pardoll DM. Mechanism-driven biomarkers to guide immune checkpoint blockade in cancer therapy. *Nat Rev Cancer* 2016;**16**:275−87.
2. Chao Y, Xu LG, Liang C, Feng LZ, Xu J, Dong ZL, et al. Combined local immunostimulatory radioisotope therapy and systemic immune checkpoint blockade imparts potent antitumour responses. *Nat Biomed Eng* 2018;**2**:611−21.
3. Auslander N, Zhang G, Lee JS, Frederick DT, Miao BC, Moll T, et al. Robust prediction of response to immune checkpoint blockade therapy in metastatic melanoma. *Nat Med* 2018;**24**:1545−9.
4. Kalbasi A, Ribas A. Tumour-intrinsic resistance to immune checkpoint blockade. *Nat Rev Immunol* 2019;**20**:1−15.
5. Darvin P, Toor SM, Nair VS, Elkord E. Immune checkpoint inhibitors: recent progress and potential biomarkers. *Exp Mol Med* 2018;**50**:1−11.
6. Lu JQ, Liu XS, Liao YP, Salazar F, Sun BB, Jiang W, et al. Nano-enabled pancreas cancer immunotherapy using immunogenic cell death and reversing immunosuppression. *Nat Commun* 2017;**8**:1−14.

7. Pozzi C, Cuomo A, Spadoni I, Magni E, Silvola A, Conte A, et al. The EGFR-specific antibody cetuximab combined with chemotherapy triggers immunogenic cell death. *Nat Med* 2016;**22**:624.
8. Wang L, Niu MY, Zheng CX, Zhao HJ, Niu XX, Li L, et al. A core−shell nanoplatform for synergistic enhanced sonodynamic therapy of hypoxic tumor *via* cascaded strategy. *Adv Healthc Mater* 2018;**7**:1800819.
9. Krysko DV, Garg AD, Kaczmarek A, Krysko O, Agostinis P, Vandenabeele P. Immunogenic cell death and DAMPs in cancer therapy. *Nat Rev Cancer* 2012;**12**:860−75.
10. Li L, Li YC, Yang CH, Radford DC, Wang JW, Janát-Amsbury M, et al. Inhibition of immunosuppressive tumors by polymer-assisted inductions of immunogenic cell death and multivalent PD-L1 cross-linking. *Adv Funct Mater* 2020;**30**:1908961.
11. Yang WJ, Zhang FW, Deng HZ, Lin LS, Wang S, Kang F, et al. Smart nanovesicle-mediated immunogenic cell death through tumor microenvironment modulation for effective photodynamic immunotherapy. *ACS Nano* 2019;**14**:620−31.
12. Lu Y, Yang YN, Gu ZY, Zhang J, Song H, Xiang GY, et al. Glutathione-depletion mesoporous organosilica nanoparticles as a self-adjuvant and co-delivery platform for enhanced cancer immunotherapy. *Biomaterials* 2018;**175**:82−92.
13. Gan SJ, Tong XN, Zhang Y, Wu JH, Hu YQ, Yuan Ah. Covalent organic framework-supported molecularly dispersed near-infrared dyes boost immunogenic phototherapy against tumors. *Adv Funct Mater* 2019;**29**:1902757.
14. He YC, Cong C, He YQ, Hao ZN, Li CH, Wang S, et al. Tumor hypoxia relief overcomes multidrug resistance and immune inhibition for self-enhanced photodynamic therapy. *Chem Eng J* 2019;**375**:122079.
15. Liu T, Liu WL, Zhang MK, Yu WY, Gao F, Li CX, et al. Ferrous-supply-regeneration nanoengineering for cancer-cell-specific ferroptosis in combination with imaging-guided photodynamic therapy. *ACS Nano* 2018;**12**:12181−92.
16. Shen ZY, Song JB, Yung BC, Zhou ZJ, Wu AG, Chen XY. Emerging strategies of cancer therapy based on ferroptosis. *Adv Mater* 2018;**30**:1704007.
17. Bao WE, Liu XW, Lv YL, Lu GH, Li F, Zhang F, et al. Nanolongan with multiple on-demand conversions for ferroptosis−apoptosis combined anticancer therapy. *ACS Nano* 2019;**13**:260−73.
18. Yang YN, Tang J, Abbaraju PL, Jambhrunkar M, Song H, Zhang M, et al. Hybrid nanoreactors: enabling an off-the-shelf strategy for concurrently enhanced chemo-immunotherapy. *Angew Chem Int Ed* 2018;**130**:11938−43.
19. Zhang F, Li F, Lu GH, Nie WD, Zhang LJ, Lv YL, et al. Engineering magnetosomes for ferroptosis/immunomodulation synergism in cancer. *ACS Nano* 2019;**13**:5662−73.
20. Li B, Hao GY, Sun B, Gu Z, Xu ZP. Engineering a therapy-induced "immunogenic cancer cell death" amplifier to boost systemic tumor tlimination. *Adv Funct Mater* 2020;**30**:1909745.
21. Bokare AD, Choi W. Review of iron-free Fenton-like systems for activating $H_2O_2$ in advanced oxidation processes. *J Hazard Mater* 2014;**275**:121−35.
22. Wang TT, Zhang H, Liu HH, Yuan Q, Ren F, Han YB, et al. Boosting $H_2O_2$-guided chemodynamic therapy of cancer by enhancing reaction kinetics through versatile biomimetic Fenton nanocatalysts and the second near-infrared light irradiation. *Adv Funct Mater* 2020;**30**:1906128.
23. Wang M, Wang DM, Chen Q, Li CX, Li ZQ, Lin J. Recent advances in glucose-oxidase-based nanocomposites for tumor therapy. *Small* 2019;**15**:1903895.
24. Li J, Burgess DJ. Nanomedicine-based drug delivery towards tumor biological and immunological microenvironment. *Acta Pharm Sin B* 2020;**11**:2110−24.
25. Feng W, Han XG, Wang RY, Gao X, Hu P, Yue WW, et al. Nanocatalysts-augmented and photothermal-enhanced tumor-specific sequential nanocatalytic therapy in both NIR-I and NIR-II biowindows. *Adv Mater* 2019;**31**:1805919.
26. Zhang YF, Yang YC, Jiang SS, Li F, Lin J, Wang TF, et al. Degradable silver-based nanoplatform for synergistic cancer starving-like/metal ion therapy. *Mater Horizons* 2019;**6**:169−75.
27. Fu LH, Qi C, Hu YR, Lin J, Huang P. Glucose oxidase-instructed multimodal synergistic cancer therapy. *Adv Mater* 2019;**31**:1808325.
28. Zhang R, Feng LZ, Dong ZL, Wang L, Liang C, Chen JW, et al. Glucose & oxygen exhausting liposomes for combined cancer starvation and hypoxia-activated therapy. *Biomaterials* 2018;**162**:123−31.
29. Chen XH, Li YX, Li SW, Gao M, Ren L, Tang BZ. Mitochondria-and lysosomes-targeted synergistic chemo-photodynamic therapy associated with self-monitoring by dual light-up fluorescence. *Adv Funct Mater* 2018;**28**:1804362.
30. Wang YQ, Liu ZY, Wang H, Meng ZJ, Wang YL, Miao WJ, et al. Starvation-amplified CO generation for enhanced cancer therapy *via* an erythrocyte membrane-biomimetic gas nanofactory. *Acta Biomater* 2019;**92**:241−53.
31. Xie W, Deng WW, Zan MH, Rao L, Yu GT, Zhu DM, et al. Cancer cell membrane camouflaged nanoparticles to realize starvation therapy together with checkpoint blockades for enhancing cancer therapy. *ACS Nano* 2019;**13**:2849−57.
32. Zhang M, Wang WT, Wu F, Zheng T, Ashley J, Mohammadniaei M, et al. Biodegradable poly (γ-glutamic acid)@glucose oxidase@carbon dot nanoparticles for simultaneous multimodal imaging and synergetic cancer therapy. *Biomaterials* 2020;**252**:120106.
33. Zhang YH, Qiu WX, Zhang M, Zhang L, Zhang XZ. $MnO_2$ motor: a prospective cancer-starving therapy promoter. *ACS Appl Mater Interfaces* 2018;**10**:15030−9.
34. Yang X, Yang Y, Gao F, Wei JJ, Qian CG, Sun MJ. Biomimetic hybrid nanozymes with self-supplied $H^+$ and accelerated $O_2$ generation for enhanced starvation and photodynamic therapy against hypoxic tumors. *Nano Lett* 2019;**19**:4334−42.
35. Lu ZJ, Gao JY, Fang C, Zhou Y, Li X, Han GR. Porous Pt nanospheres incorporated with GOx to enable synergistic oxygen-inductive starvation/electrodynamic tumor therapy. *Adv Sci* 2020;**7**:2001223.
36. Sun YX, Zhao DY, Wang G, Wang Y, Cao LL, Sun J, et al. Recent progress of hypoxia-modulated multifunctional nanomedicines to enhance photodynamic therapy: opportunities, challenges, and future development. *Acta Pharm Sin B* 2020;**8**:1382−96.
37. Nam J, Son SJ, Ochyl LJ, Kuai R, Schwendeman A, Moon JJ. Chemo-photothermal therapy combination elicits anti-tumor immunity against advanced metastatic cancer. *Nat Commun* 2018;**9**:1−13.
38. Chen Q, Xu LG, Liang C, Wang C, Peng R, Liu Z. Photothermal therapy with immune-adjuvant nanoparticles together with checkpoint blockade for effective cancer immunotherapy. *Nat Commun* 2016;**7**:1−13.
39. Zhou ZG, Zhang BL, Wang SS, Zai WJ, Yuan AH, Hu YQ, et al. Perfluorocarbon nanoparticles mediated platelet blocking disrupt vascular barriers to improve the efficacy of oxygen-sensitive antitumor drugs. *Small* 2018;**14**:1801694.
40. Liang X, Ye XY, Wang C, Xing CY, Miao QW, Xie ZJ, et al. Photothermal cancer immunotherapy by erythrocyte membrane-coated black phosphorus formulation. *J Control Release* 2019;**296**:150−61.
41. Hu JJ, Liu MD, Gao F, Chen Y, Peng SY, Li ZH, et al. Photo-controlled liquid metal nanoparticle-enzyme for starvation/photothermal therapy of tumor by win-win cooperation. *Biomaterials* 2019;**217**:119303.
42. Tang ZM, Zhang HL, Liu YY, Ni DL, Zhang H, Zhang JW, et al. Antiferromagnetic pyrite as the tumor microenvironment-mediated nanoplatform for self-enhanced tumor imaging and therapy. *Adv Mater* 2017;**29**:1701683.
43. Yang WT, Xiang CY, Xu Y, Chen SZ, Zeng WW, Liu K, et al. Albumin-constrained large-scale synthesis of renal clearable ferrous sulfide quantum dots for T1-Weighted MR imaging and phototheranostics of tumors. *Biomaterials* 2020;**255**:120186.
44. Yang WT, Shi XD, Shi YX, Yao DF, Chen SZ, Zhou X, et al. Beyond the roles in biomimetic chemistry: an insight into the intrinsic catalytic activity of an enzyme for tumor-selective phototheranostics. *ACS Nano* 2018;**12**:12169−80.
45. Jin QT, Liu JJ, Zhu WJ, Dong ZL, Liu Z, Cheng L. Albumin-assisted synthesis of ultrasmall $FeS_2$ nanodots for imaging-guided photothermal enhanced photodynamic therapy. *ACS Appl Mater Interfaces* 2018;**10**:332−40.

46. Minchinton AI, Tannock IF. Drug penetration in solid tumours. *Nat Rev Cancer* 2006;**6**:583−92.
47. Peng JR, Yang Q, Xiao Y, Shi K, Liu QY, Hao Y, et al. Tumor microenvironment responsive drug-dye-peptide nanoassembly for enhanced tumor-targeting, penetration, and photo-chemo-immunotherapy. *Adv Funct Mater* 2019;**29**:1900004.
48. Yu WQ, Liu R, Zhou Y, Gao HL. Size-tunable strategies for a tumor targeted drug delivery system. *ACS Cent Sci* 2020;**6**:100−16.
49. Zhou ZW, Liu YD, Zhang MH, Li CZ, Yang RX, Li J, et al. Size switchable nanoclusters fueled by extracellular ATP for promoting deep penetration and MRI-guided tumor photothermal therapy. *Adv Funct Mater* 2019;**29**:1904144.
50. An L, Yan CG, Mu XL, Tao C, Tian QW, Lin JM, et al. Paclitaxel-induced ultrasmall gallic acid-Fe@BSA self-assembly with enhanced MRI performance and tumor accumulation for cancer theranostics. *ACS Appl Mater Interfaces* 2018;**10**:28483−93.
51. Xie CK, Cen D, Ren ZH, Wang YF, Wu YJ, Li X, et al. FeS@BSA nanoclusters to enable $H_2S$-amplified ROS-based therapy with MRI guidance. *Adv Sci* 2020;**7**:1903512.
52. Chen Q, Chen JW, Liang C, Feng LZ, Dong ZL, Song XJ, et al. Drug-induced co-assembly of albumin/catalase as smart nano-theranostics for deep intra-tumoral penetration, hypoxia relieve, and synergistic combination therapy. *J Control Release* 2017;**263**:79−89.
53. Yu SG, Chen ZW, Zeng XA, Chen XS, Gu Z. Advances in nanomedicine for cancer starvation therapy. *Theranostics* 2019;**9**:8026.
54. Gao SS, Lin H, Zhang HX, Yao HL, Chen Y, Shi J. Nanocatalytic tumor therapy by biomimetic dual inorganic nanozyme-catalyzed cascade reaction. *Adv Sci* 2019;**6**:1801733.
55. Obeid M, Tesniere A, Ghiringhelli F, Fimia GM, Apetoh L, Perfettini JL, et al. Calreticulin exposure dictates the immunogenicity of cancer cell death. *Nat Med* 2007;**13**:54−61.
56. Zhang ZW, Wang H, Tan T, Li J, Wang ZW, Li YP. Rational design of nanoparticles with deep tumor penetration for effective treatment of tumor metastasis. *Adv Funct Mater* 2018;**28**:1801840.
57. Song WT, Shen LM, Wang Y, Liu Q, Goodwin TJ, Li JJ, et al. Synergistic and low adverse effect cancer immunotherapy by immunogenic chemotherapy and locally expressed PD-L1 trap. *Nat Commun* 2018;**9**:1−11.